

# High geomagnetic field intensity recorded by anorthosite xenoliths requires a strongly powered late Mesoproterozoic geodynamo

Yiming Zhang<sup>a,1</sup>, Nicholas L. Swanson-Hysell<sup>a</sup>, Margaret S. Avery<sup>a,b</sup>, and Roger R. Fu<sup>c</sup>

<sup>a</sup>Department of Earth and Planetary Science, University of California, Berkeley, CA, 94720; <sup>b</sup>U.S. Geological Survey, Moffett Field, CA, 94025; <sup>c</sup>Department of Earth and Planetary Sciences, Harvard University, Cambridge, MA, 02138

This manuscript was compiled on February 25, 2022

1 **Obtaining estimates of Earth's magnetic field strength in deep time**  
2 is complicated by non-ideal rock magnetic behavior in many igneous  
3 rocks. In this study, we target anorthosite xenoliths that cooled  
4 and acquired their magnetization within ca. 1092 Ma shallowly em-  
5 placed diabase intrusions of the North American Midcontinent Rift.  
6 In contrast to the diabase which fails to provide reliable paleointen-  
7 sity estimates, the anorthosite xenoliths are unusually high-fidelity  
8 recorders yielding high-quality, single-slope paleointensity results  
9 that are consistent at specimen and site levels. An average value of  
10 ~82 ZAm<sup>2</sup> for the virtual dipole moment from the anorthosite xeno-  
11 liths, with the highest site-level values up to ~127 ZAm<sup>2</sup>, are higher  
12 than that of the dipole component of Earth's magnetic field today and  
13 rival the highest values in the paleointensity database. Such high in-  
14 tensities recorded by the anorthosite xenoliths require the existence  
15 of a strongly powered geodynamo at the time. Together with pre-  
16 vious paleointensity data from other Midcontinent Rift rocks, these  
17 results indicate that a dynamo with strong power sources persisted  
18 for more than 14 million years ca. 1.1 Ga. These data are incon-  
19 sistent with there being a progressive monotonic decay of Earth's  
20 dynamo strength through the Proterozoic Eon and could challenge  
21 the hypothesis of a young inner core. The multiple observed paleo-  
22 intensity transitions from weak to strong in the Paleozoic and the  
23 Proterozoic present challenges in identifying the onset of inner core  
24 nucleation based on paleointensity records alone.

absolute paleointensity | anorthosite | geodynamo | Proterozoic | inner core

Earth's magnetic field is the result of convective flow of liquid iron-alloy in Earth's outer core. At present day, the geodynamo is collectively powered by heat flow across the core-mantle boundary (CMB) and from the crystallization of the solid inner core from the liquid outer core which provides latent heat and compositional buoyancy (1). However, while paleomagnetic studies have found that a dynamo field has existed since at least 3.4 billion years ago (2–4), Earth's inner core likely crystallized more recently. Estimates of the timing of the initial crystallization of Earth's inner core are interconnected with estimates for the core's thermal conductivity. Higher conductivity values imply faster cooling rates, which in turn imply that the threshold for the freezing of the inner core happened more recently (5). While some estimates of these values are consistent with an inner core age >3 Ga (6, 7), other estimates have implied higher thermal conductivity values and an age for the inner core that is less than 1.5 Ga (8–12), with some suggesting even younger ages (<700 Ma; 13, 14). Given that estimates for the core's thermal conductivity continue to be debated, it is crucial to use observational records as an independent constraint on the thermal evolution of Earth's

core and mantle.

Paleomagnetic records from ancient rocks are one of the few types of observational data that have the potential to provide constraints on the thermal evolution of Earth's core. Evidence for a persistent magnetic field through the Proterozoic, for example, likely necessitates the existence of plate tectonics that sustained core-mantle boundary heat flow (15). However, strikingly low estimates of geomagnetic field strengths have been obtained ca. 565 Ma during the Ediacaran Period (16–18) and ca. 370 Ma during the Devonian Period (19–21), potentially indicating unusual periods of core dynamo activity at those times. The Ediacaran data have been interpreted to indicate that there was a progressively decaying field up to that time that was soon followed by initial crystallization of the inner core (16). Sparse data in the Proterozoic Era (2500 to 539 Ma) and the reality of high variability in Phanerozoic Era records (539 to 0 Ma) necessitate additional data to evaluate interpreted trends.

Determinations of the absolute value of ancient geomagnetic field strength rely on igneous rocks that acquire thermal remanent magnetizations as they cool. These magnetizations need to be unmodified by subsequent heating or chemical alteration in order to maintain a record of the ancient geomagnetic field from the time of cooling. Intratemporal

## Significance Statement

Acquiring high-fidelity ancient magnetic field intensity records from rocks is crucial for constraining the long-term evolution of Earth's core. However, robust estimates of ancient field strengths are often difficult to recover due to alteration or non-ideal behavior. We use anorthosites that formed in the deep crust and were brought to the near surface where they acquired thermal remanent magnetizations. These anorthosites have experienced minimal post-formation alteration and yield high-quality paleointensity estimates. In contrast to scenarios of a progressively decaying field leading up to late nucleation of Earth's inner core, these data record a strong field 1.1 Ga. A strong field that persisted over a 14-million-year interval indicates the existence of appreciable power sources for Earth's dynamo during the late Mesoproterozoic.

Author contributions: Y.Z. and N.L.S.-H. designed research; Y.Z., N.L.S.-H. and M.S.A conducted fieldwork and sampling; Y.Z. and N.L.S.-H. conducted and analyzed rock magnetic experiments; Y.Z. performed petrography and electron microscopy; R.R.F. contributed to magnetic imaging data analyses; Y.Z. and N.L.S.-H. wrote the paper with input from M.S.A. and R.R.F.

The authors declare no conflict of interest.

<sup>1</sup>To whom correspondence should be addressed. E-mail: yimingzhang@berkeley.edu

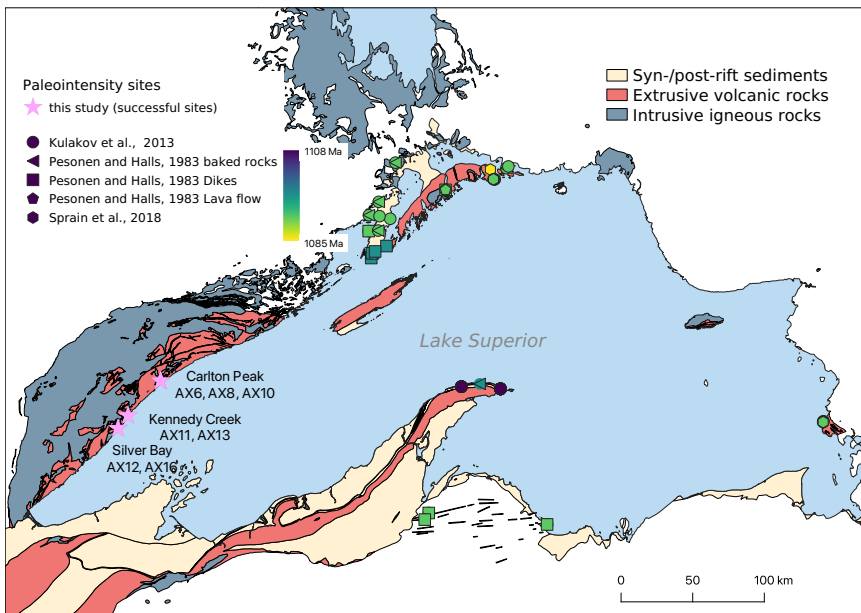


**Fig. 1.** Simplified geologic map of the Lake Superior region showing the distribution of rocks associated with the late Mesoproterozoic Midcontinent Rift. Purple stars mark sites with paleointensity results that passed the selection criteria from this study. Paleomagnetic sites from 22–24 are categorized by lithology. All sites from 22–24 are color-coded by their ages.

46 magmatic events are an important target for determination  
47 of ancient paleointensity as they can be well-preserved within  
48 continental interiors. This interior position results in them  
49 typically being distant from tectonic events along continental  
50 margins that can drive alteration through heat and fluids.  
51 However, intraplate magmatism associated with large igneous  
52 provinces is typically of geologically short duration with the  
53 bulk of magmatic products emplaced within 1 Myr or less  
54 (25). The Midcontinent Rift (Fig. 1) is an exception as it is  
55 a large igneous province where magmatism lasted ~25 Myr  
56 from ca. 1109 Ma to 1084 Ma during which there were pulsed  
57 intervals of more rapid activity (26). Additionally, extension  
58 ceased in the Midcontinent Rift prior to lithospheric separation,  
59 preserving volcanic, intrusive, and sedimentary rocks  
60 of the rift within the continental interior. As a result, rocks  
61 of the rift have unusually simple paleomagnetic behavior for  
62 their greater than one billion-year-old age and paleomagnetic  
63 data from rift rocks forms a central record of Mesoproterozoic  
64 paleogeography (15). The duration of magmatic activity  
65 within the Midcontinent Rift is longer than the entire 20.4  
66 Myr long Neogene Period such that it enables an extended  
67 well-preserved window into the intensity of Earth's magnetic  
68 field in the late Mesoproterozoic.

69 Despite the excellent preservation of the rocks, non-ideal  
70 paleointensity behaviors have challenged the interpretation of  
71 many previous paleointensity results from the Midcontinent  
72 Rift (22–24). The most trusted type of paleointensity estimate  
73 is that obtained through experiments in which the primary  
74 natural thermal remanent magnetization is progressively re-  
75 placed by a laboratory magnetization that is imparted in a  
76 known field with internal consistency checks (such as in IZZI-  
77 style Thellier experiments; 27). In such Thellier paleointensity  
78 experiments, one typical departure from ideal behavior due to  
79 the presence of nonuniformly magnetized grains (with either  
80 multidomain (28) or vortex states (29)) is sagging or double-  
81 slopes as visualized in Arai plots that show thermal remanent  
82 magnetization (TRM) acquired versus natural remanent mag-  
83 netization (NRM) lost. For such data, distinct paleointensity  
84 estimates may be calculated depending on the interpreter's

choice of slope. Typically, such non-ideal behavior would result  
85 in a higher paleointensity estimate from the steeper-sloped  
86 low-temperature portion of the experiment and a lower paleo-  
87 intensity estimate from the high-temperature portion. For  
88 example, in data from the Midcontinent Rift, ref. 22 used  
89 the low-temperature slope as the best representation of the  
90 past magnetic field strength (likely overestimating the field  
91 strength) whereas ref. 23 used the high-temperature slope  
92 (likely underestimating the field strength). Such non-ideal  
93 results were rejected by ref. 24 who applied stricter paleo-  
94 intensity selection criteria, but as a result had few accepted  
95 sites.

96 In this study, we target a unique rock type—high-purity  
97 anorthosite xenoliths. Anorthosites are cumulate rocks com-  
98 posed dominantly of the mineral plagioclase. They are attrac-  
99 tive targets for paleomagnetic study as plagioclase crystals can  
100 enshroud magnetic inclusions from alteration with alteration of  
101 the plagioclase crystals themselves not resulting in the forma-  
102 tion of secondary iron oxides in contrast with mafic minerals  
103 such as olivine. The anorthosite xenoliths targeted in this  
104 study were brought to the near surface in magma that formed  
105 hypabyssal (shallowly emplaced) intrusions of the Beaver River  
106 diabase (30). They cooled and acquired their magnetizations  
107 in conjunction with the host diabase at a paleolatitude of  
108  $22^\circ \pm 2^\circ$  (calculated from the paleomagnetic pole of the coeval  
109 Portage Lake Volcanics; 30, 31). Paleointensity experiments  
110 on the anorthosite xenoliths have a high success rate, yielding  
111 consistent specimen- and site-level paleointensity results. Rock  
112 magnetic data reveal that the anorthosite xenoliths have low  
113 anisotropy of thermal remanent magnetization (TRM) and  
114 can acquire TRM linearly within the range of relevant field  
115 strengths. Magnetic imaging shows that the anorthosite spec-  
116 iments have dominant magnetic carriers within and interstitial  
117 to plagioclase crystals without strong preferred orientations.  
118 These single-slope, high-quality paleointensity data, together  
119 with other high-quality paleointensity records during the pro-  
120 tracted Midcontinent Rift magmatic activity, require that  
121 there was a strong late Mesoproterozoic geodynamo.

123 **Background on anorthosite xenoliths of the Beaver  
124 River diabase**

125 While magmatic activity within the Midcontinent Rift was  
126 protracted, there were intervals of particularly rapid volcanism and voluminous emplacement of intrusions (26). The  
127 ca. 1092 Ma Beaver Bay Complex in northern Minnesota  
128 punctuates one such period of magmatism during the main  
129 stage of Midcontinent Rift activity. The magma that formed  
130 the 1091.7±0.2 Ma Beaver River diabase dikes and sills of  
131 the Beaver Bay Complex transported numerous anorthosite  
132 xenoliths that have short-axis diameters up to 180 meters  
133 via wide conduits (32, 33). These anorthosite xenoliths are  
134 plagioclase cumulates that formed comagmatically with the  
135 host diabase in the lower crust—an interpretation confirmed  
136 by U-Pb zircon geochronology (30).

137 Thermal modeling results and paleomagnetic directional  
138 data show the anorthosite xenoliths to have acquired thermal  
139 remanent magnetizations while cooling with the Beaver River  
140 diabase (30). Step-wise thermal demagnetization data show  
141 the anorthosite xenoliths to have dominantly single-component  
142 magnetization that often unblock sharply within temperature  
143 ranges between 500°C and 580°C, consistent with magnetiza-  
144 tion held by low-titanium titanomagnetite (30).

145 **Results and Interpretations**

146 **Petrography and magnetic imaging of anorthosite xenoliths.**

147 The dominantly monomineralic anorthosite xenoliths within  
148 the Beaver River diabase often have granoblastic texture char-  
149 acterized by equigranular crystals with weakly developed petro-  
150 fabrics (Fig. 2A). Plagioclase crystals within coarse-grained  
151 intrusions often contain abundant elongate Fe-Ti oxide inclu-  
152 sions that are visible through optical microscopy (34). The  
153 Beaver River anorthosite xenoliths lack such large (10s of  $\mu\text{m}$ )  
154 oxide inclusions such that oxides are not visible within the  
155 plagioclase crystals through optical microscopy (Fig. 2C).  
156 However, magnetic imaging using a quantum diamond mi-  
157 croscope (QDM) shows that there are magnetic remanence  
158 carriers within the plagioclase crystals (Fig. 2E, G). To high-  
159 light these distinct aspects of the Beaver River anorthosite  
160 xenoliths, we present petrographic and magnetic imaging data  
161 from the Beaver River anorthosite as well as a sample of an  
162 anorthosite from the Duluth Complex Anorthositic Series—an  
163 older intrusive complex within the Midcontinent Rift that was  
164 not targeted for paleointensity experiments in this study (Fig.  
165 2). In contrast to the Beaver River anorthosite, the plagi-  
166 olase of the Duluth Complex anorthosites typically develop  
167 interlocking textures that display pronounced igneous folia-  
168 tion (Fig. 2B). In addition, there are abundant Fe-Ti oxide  
169 needles within the Duluth Complex plagioclase grains that  
170 are typically aligned with the [001] axes of the crystals (Fig.  
171 2D). Magnetic imaging confirms that these magnetite needles  
172 have magnetic moments oriented along their long axes (Fig.  
173 2F, H). As a result of this shape anisotropy, magnetization  
174 is acquired at angles highly oblique to applied fields (Figure  
175 2F). In an experiment where a second orthogonal field was  
176 applied, the first isothermal remanent magnetizations (IRM)  
177 of a set of magnetite needles within a plagioclase grain either  
178 fail to rotate or flip by 180°. When they flip, they remain in a  
179 direction that is oblique to the applied field direction dictated  
180 by shape anisotropy (Fig. 2F, H). These experiments enable  
181 novel visualization of the grain-scale magnetic anisotropy of

182 elongated exsolved (titanio)magnetite inclusions within pla-  
183 gioclase that leads to magnetic anisotropy observed at the  
184 bulk sample scale (34, 35). In contrast, the remanent mag-  
185 netizations of the ferromagnetic grains imaged in the Beaver  
186 River anorthosite xenoliths, targeted for paleointensity in this  
187 study, align with the applied field directions indicating min-  
188 imal remanence anisotropy (Fig. 2E, G). The relative lack  
189 of petrofabrics and minimal grain-scale magnetic anisotropy  
190 make the Beaver River anorthosite xenoliths a particularly  
191 compelling target for paleointensity experiments.

192 **Paleointensity.** Following IZZI-style paleointensity exper-  
193 iments (27), 40 from a total of 86 anorthosite specimens and 0  
194 out of a total of 69 diabase specimens passed our paleointensity  
195 result selection criteria (see Materials and Methods section).  
196 7 anorthosite sites and no diabase sites have specimen results  
197 that pass these selection criteria. Example NRM/TRM (Arai)  
198 plots are shown in Figure 3. Summary specimen absolute  
199 paleointensity estimates and site-level mean paleointensity val-  
200 ues are plotted in Figure 4 (and provided in Table S1) where  
201 each site is an individual anorthosite xenolith. The paleointen-  
202 sity quality index ( $Q_{PI}$ ; 36) for the anorthosite xenolith  
203 sites are all 5 or 6 (Table S2). The cooling rate-corrected  
204 absolute paleointensity estimates from the anorthosite xeno-  
205 liths have a mean of  $38.28 \pm 11.92 \mu\text{T}$ . The site-mean virtual  
206 dipole moment is  $\sim 82 \text{ ZAm}^2$  ( $10^{21} \text{ Am}^2$ ) ca. 1092 Ma. All  
207 measurement-level paleointensity experiment data are avail-  
208 able within the MagIC database (<https://earthorg/MagIC/19462/8d3c2258-11ae-4830-b99f-3f6b02eceb7e>; *this private link is provided for the purpose of review; the url will be updated when a doi is generated for this manuscript*).

209 Typical paleointensity experimental data of the anorthosite  
210 specimens have straight, single-slope NRM/TRM plots and  
211 the accepted fractions of temperature steps span over the  
212 origin-trending, primary remanence components (Fig. 3). We  
213 accept specimen- and site-level absolute paleointensity results  
214 from those anorthosite xenoliths that pass the selection crite-  
215 ria. Other anorthosite xenoliths and diabase specimens failed  
216 the selection criteria largely because of double-slope or sagging  
217 behavior (fail FRAC selection; see Materials and Methods sec-  
218 tion), poor pTRM checks, and sometimes zigzagging behaviors  
219 superimposed on top of sagging behavior (fail SCAT, DANG  
220 selection; see Materials and Methods section; Fig. 3). A 20  
221 mT alternating field treatment after in-field heating steps was  
222 applied to some specimens, but it did not result in significant  
223 changes in the experimental results for the anorthosite xenolith  
224 or diabase specimens (Fig. 4; Supporting Information).

225 In addition to estimating paleointensity values by introduc-  
226 ing a set of selection criteria to filter our experiment results,  
227 we apply an independent method from ref. 39 with all experi-  
228 mental data regardless of their NRM/TRM plot statistics to  
229 perform bias corrected estimation of paleointensity (BiCEP).  
230 This Bayesian probabilistic method is based on an assumption  
231 that paleointensity estimates from specimens that come from  
232 a same cooling unit are distributed around a true paleointen-  
233 sity value with the various deflections being expressed as  
234 the curvature parameter of the NRM/TRM plot (40). The  
235 posterior paleointensity distributions from these sites with  
236 high-quality specimen-level data are in agreement with the  
237 site-level averages developed using the selection criteria ap-  
238 proach (Fig. 4; Fig. S1). Overall, the high-quality results from  
239 the anorthosite xenoliths of the Beaver River diabase indicate  
240

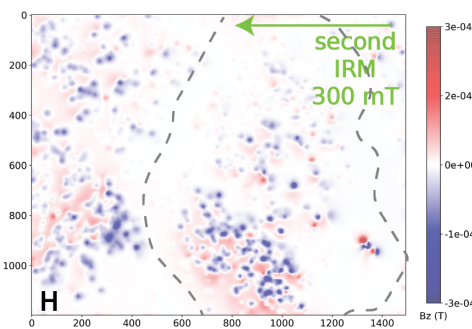
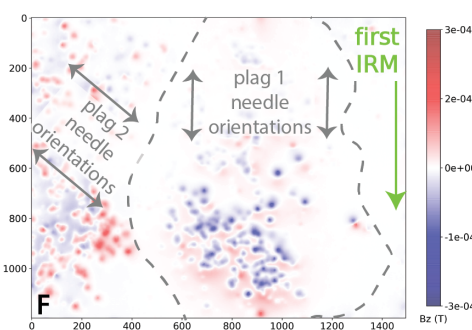
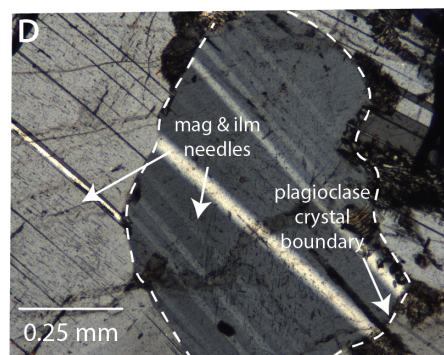
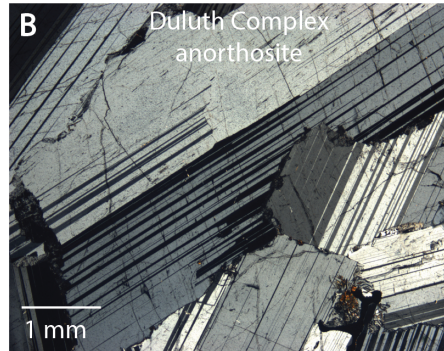
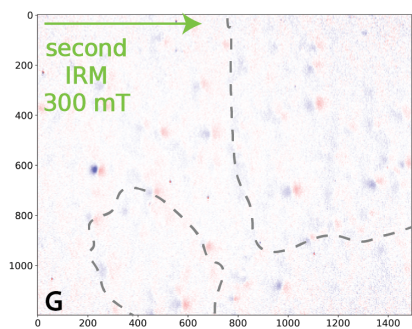
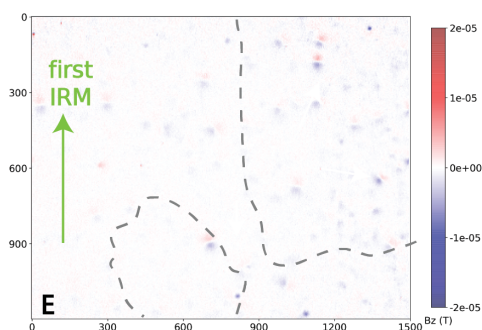
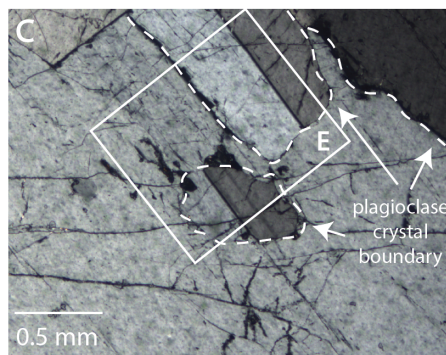


**Fig. 2.** Thin section petrographic images (A,B,C,D) and magnetic maps (E,F,G,H) of anorthosite from the Beaver River anorthosite xenolith in the Silver Bay region from which paleomagnetic site AX16 and geochronology sample MS99033 were collected (left column; 30) and a distinct anorthosite from the Duluth Complex Anorthositic Series (right column). The Duluth Complex anorthosites were not targeted for paleointensity experiments in this study given complexities associated with more pronounced fabrics. Cross-polarized petrographic images of the Beaver River anorthosite (A,C) reveal plagioclase with a granoblastic texture of crystals that are largely free of large opaque inclusions. In contrast, plagioclase crystals in the Duluth Complex anorthosite have euhedral, interlocking crystals with an igneous foliation (B) and the plagioclase crystals contain abundant Fe-Ti oxide needles that have preferred orientations that are often parallel with the [001] axis of the plagioclase. Maps of the vertical component of magnetic field ( $B_z$ ) developed with a quantum diamond microscope (QDM) show relatively weak magnetic sources within plagioclase crystals in the Beaver River anorthosite (in E) relative to the strongly magnetic large oxide needles within Duluth Complex plagioclase (in F). The  $B_z$  color scale is an order of magnitude greater in the Duluth Complex anorthosite maps (F, H) than the maps for the Beaver River anorthosite (E, G). (E to G) and (F to H) show experiments performed on both samples where we apply a first field along the y axis of the field of view and then apply a second field of 300 mT orthogonal to the first field direction. The remanence magnetizations acquired by both anorthosites were mapped after the application of each field. The magnetic images show that remanence magnetizations of Beaver River anorthosite (i.e. the individual dipoles visible with paired red  $+B_z$  and blue  $-B_z$  lobes) align well with the first applied field direction (E) and then rotated to align with the second applied field direction indicating minimal anisotropic behavior (G). In contrast, the remanence magnetizations carried by the magnetic needles in plagioclase 1 of the Duluth anorthosite xenolith align well with the first applied field but those in plagioclase 2 acquired an oblique remanence direction with respect to the field direction (F). After the application of an orthogonal 300 mT external field, magnetization of those needles in plagioclase 1 did not change direction due to strong shape anisotropy whereas the magnetization of needles in plagioclase 2 flipped, but with the acquired remanence remaining oblique to the field direction (H). This experiment illustrates that the Beaver River anorthosite xenolith has much lower magnetic anisotropy than the Duluth anorthosite xenolith. The unit of the axes in the QDM maps are in  $\mu\text{m}$ .

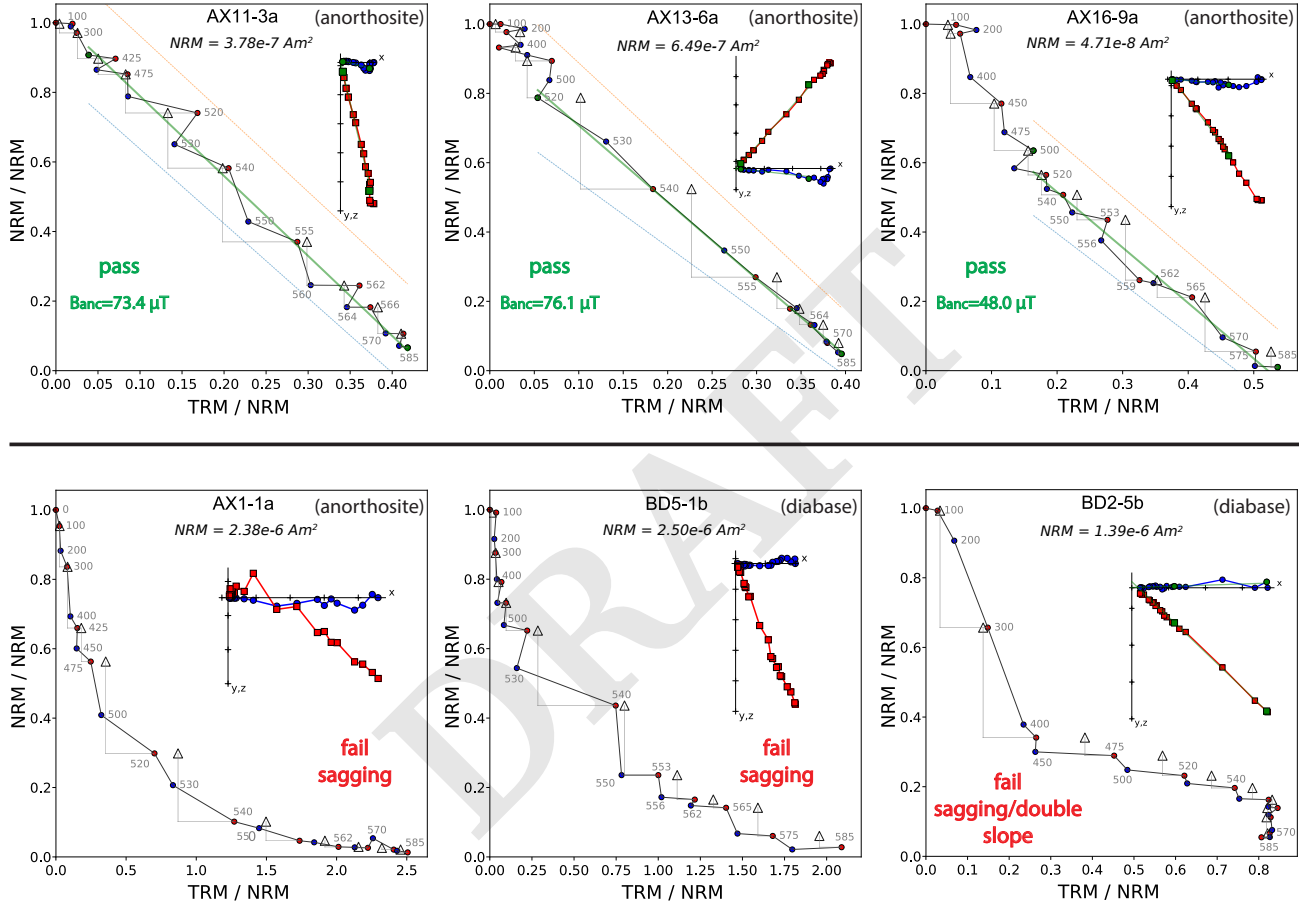


**Fig. 3.** Example results of paleointensity experiments are displayed on Arai plots and zero-field heating results are shown on inset orthogonal plots (Zijderveld plots) for anorthosite and diabase specimens. Red (blue) circles indicate zero-field/in-field (in-field/zero-field) steps 'ZI' ('IZ'). Triangles mark partial thermal remanent magnetization (pTRM) checks. Blue and red squares in the Zijderveld plots are X-Y and X-Z projections, respectively, of the NRMs in specimen coordinates. Plots on the top row show successful specimen paleointensity results with straight, single-slope behaviors that pass our selection criteria. The green lines represent fits for the dominant single-slope component that passes the acceptance criteria and gives an estimate of the ancient field strength ( $B_{anc}$ ). The plots for anorthosite specimens AX1-1a and diabase BD5-1b on the bottom row show non-ideal sagging behaviour that fails our acceptance criteria. Specimen BD2-5a is an example where the data appear linear with distinct slopes in the low and high temperature ranges such that it could pass less restrictive selection criteria, particularly if a narrower temperature range was used for the experiment. Data analysis and visualization was conducted using PmagPy (37).

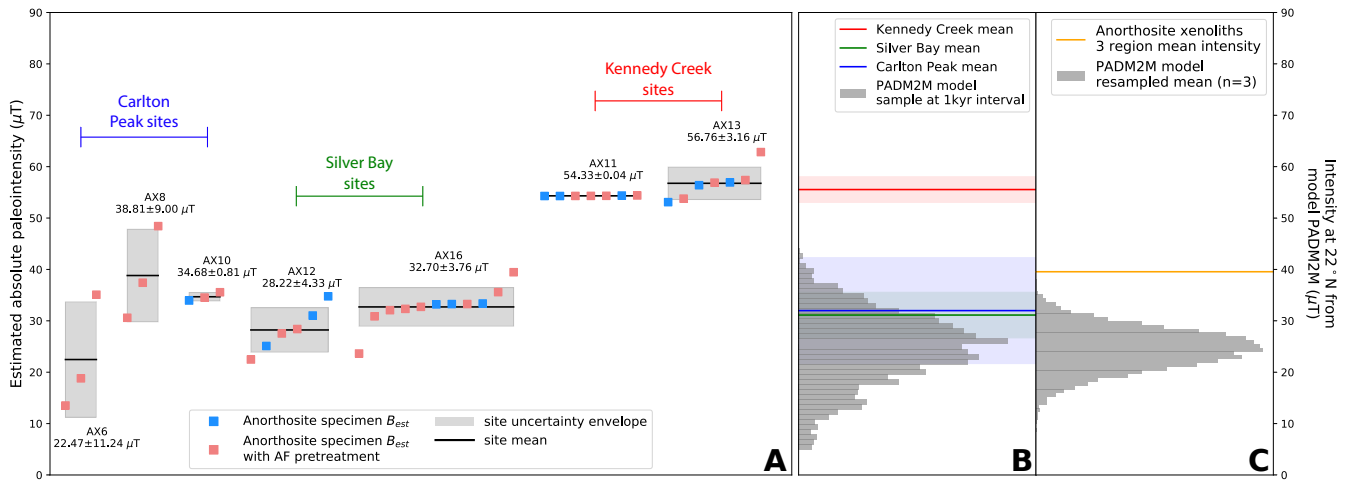


**Fig. 4.** A) Summary plot of individual specimen absolute paleointensity results (square symbols) and their averages and standard deviations at site level (black bars with grey 1 $\sigma$  uncertainty boxes) where each 'AX' site is an individual anorthosite xenolith within the Beaver River diabase. All results are corrected for cooling rate with a factor of 0.74. The sites with successful experiments come from 3 regions (Carlton Peak, Silver Bay, Kennedy Creek) which would have cooled at distinct times yielding similar estimates within the each region with differences between regions. B) Regional means calculated from the specimen-level data are compared to the distribution of intensities calculated from a paleomagnetic axial dipole moment model for the past 2 million years (PADM2M; 38) at the latitude corresponding to the paleolatitude of study region (22°N). C) The mean of the 3 regional means is compared to means calculated from 3 random values drawn from the PADM2M model (38). The distribution represents a total of 10,000 iterations of taking 3 random draws and calculating the mean. These comparisons highlight that these paleointensity values are strong in relation to the geomagnetic field over the past 2 million years.

that the anorthosite xenoliths record a high geomagnetic field ca. 1092 Ma.

## Rock magnetism.

**Coercivity.** Additional rock magnetic data support that the anorthosite specimens that pass the paleointensity selection criteria have dominant magnetic remanence carriers with magnetic properties similar to stoichiometric, non-interacting, single domain magnetite, whereas anorthosite samples that failed the paleointensity result selection and all diabase samples have more pronounced populations of non-ideal carriers. Magnetic property measurement system (MPMS) data show both diabase and anorthosite contain (titano)magnetite as evidenced through the presence of the Verwey transition (Fig. S2; 41, 42). Anorthosite specimens from sites that yield successful paleointensity results have Verwey transition temperatures near 120 K as expected for stoichiometric magnetite with minimal Ti (43). However, diabase and anorthosite specimens that did not pass our paleointensity selection typically have Verwey transitions that are suppressed toward lower temperatures (Fig. S2), indicating that magnetite grains in the specimens either have relatively higher Ti content or have been partially oxidized (43). Another difference is that samples which pass paleointensity selection criteria have distinctly higher average median destructive field values than other anorthosite and diabase specimens (Fig. 5). Single-component fits for coercivity spectra (44) show that anorthosites that yielded successful paleointensity results can have magnetic grain populations with peak coercivity around 80 mT (Fig. 5). In contrast, other anorthosite and diabase tend to have lower peak coercivities (~30 mT). This result is consistent with an interpretation that a population of magnetic grains with more multidomain-like behavior is responsible for the non-ideal paleointensity behaviors during experiments on such specimens (45).

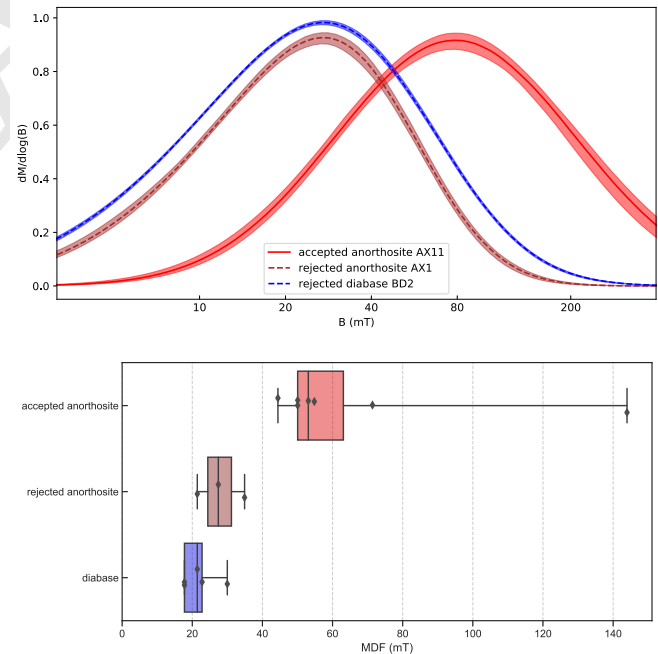


**Fig. 5.** Top: Example coercivity spectra of anorthosite and diabase specimens from sites that pass or fail our paleointensity selection criteria. Bottom: Box plots of median destructive field (MDF) values for all anorthosite and diabase specimens with single-component coercivity unmixing results. Both plots show that anorthosite specimens that pass paleointensity selection criteria have higher coercivities consistent with a higher portion of single-domain-like magnetite grains than the other anorthosite specimens and the diabase.

**277 Bulk TRM anisotropy.** Significant remanence anisotropy has been  
278 documented to exist within certain anorthositic rocks that  
279 form in layered intrusive complexes (34, 35). Strong rema-  
280 nence anisotropy associated with the igneous foliation devel-  
281 oped within anorthosite from the Stillwater Complex has been  
282 shown to lead to significant overestimation or underestimation  
283 of paleointensity values depending on the relative orienta-  
284 tions between the fabrics and an applied magnetic field (35).  
285 To assess whether our paleointensity estimates are biased by  
286 bulk remanence anisotropy, we calculated the gamma statis-  
287 tic, which is the angular difference between the last pTRM  
288 step of paleointensity experiment and the applied field direc-  
289 tion. The results show that the anorthosite specimens used  
290 for paleointensity experiment have low gamma values ranging  
291 from 0.9° to 11.9°, with a median value of 4.2° (Table S1).  
292 Because these anorthosite specimens were oriented at various  
293 directions with respect to the outcrops, the angle between the  
294 applied lab field direction during paleointensity experiments  
295 with respect to any fabrics within the anorthosites specimens  
296 are expected to cover a wide range of angles. These gamma  
297 values of the anorthosite xenolith bulk specimens are similar  
298 to those of Midcontinent Rift volcanics (24). Therefore, the  
299 bulk Beaver River anorthosite xenoliths do not have signifi-  
300 cant remanence anisotropy. Paleodirectional data from our  
301 anorthosite xenoliths further support that they have minimal  
302 remanence anisotropy as their site mean directions closely  
303 match those of the Beaver River diabase hosts without devi-  
304 ating due to a fabric (30). These bulk results are consistent  
305 with the data from the QDM magnetic map experiments that  
306 reveal minimal remanence anisotropy (Fig. 2).

**307 Considering secular variation and cooling rate.** To best char-  
308 acterize the geomagnetic axial dipole field intensity during a  
309 certain time period a paleointensity dataset should cover a  
310 sufficient amount of time such that paleosecular variations of  
311 the geomagnetic field are averaged. Thermal modeling results  
312 from ref. 30 indicate that the Beaver River anorthosite xeno-  
313 liths were heated to tholeiitic magma temperature (~1100°C)  
314 and acquired thermal remanent magnetization during cooling  
315 with their diabase host on a time scale of a thousand years,  
316 partially averaging secular variation within single sites. An-  
317 other consequence of the anorthosite xenoliths having cooled  
318 in the interior of thick diabase intrusions is that slow cooling  
319 rates can bias paleointensity estimates toward higher values.  
320 Large differences in cooling rates between acquisition of an  
321 NRM in nature versus a TRM in the lab can result in over-  
322 estimated paleointensities for single domain grains (46–48).  
323 From the thermal history model of ref. 30, we can estimate  
324 the duration over which the diabase and anorthosite cooled  
325 from the Curie temperature of magnetite (~580°C) to the  
326 time when they fully blocked in their characteristic natural  
327 remanence magnetization (~500°C; 30). We find the cooling  
328 time to be on the order of ~1 kyr, which corresponds to a  
329 cooling rate of  $\sim 1.6 \times 10^{-9} \text{ }^{\circ}\text{C s}^{-1}$ . In contrast, the lab cool-  
330 ing rate is much faster through the same temperature interval  
331 with an estimated cooling rate of  $\sim 1.3 \times 10^{-1} \text{ }^{\circ}\text{C s}^{-1}$ . The  
332 significant cooling rate difference leads to a predicted ~36%  
333 overestimate of true ancient field following the model of 47  
334 (Fig. S3). This estimate on cooling rate effect is similar to  
335 the value of ~35% overestimate derived from the model of ref.  
336 48. We therefore correct our paleointensity results by a factor  
337 of 0.74. The cooling rate-corrected specimen paleointensity

estimates together with specimen- and site-level means are  
338 shown in Fig. 4.

Anorthosite xenoliths have paleointensity results that are  
339 consistent within small regions, but vary between regions.  
340 Anorthosite AX12 and AX16 in the Silver Bay area were  
341 emplaced ~450 meters apart and have indistinguishable pa-  
342 leointensity estimates (Figs. 1 and 4). ~10 km to the north,  
343 anorthosite xenoliths AX11 and AX13 in the Kennedy Creek  
344 area were also emplaced closely (separated by ~125 meters)  
345 and yield similar values to one another, but distinct paleointen-  
346 sity estimates from those of AX12 and AX16 (Figs. 1 and  
347 4). ~30 km further to the north in the Carlton Peak region,  
348 AX6, AX8, and AX10 are anorthosite xenoliths within 10  
349 meters of one another and also yield similar paleointensity  
350 estimates albeit with relatively large uncertainties (Fig. 4).  
351 The anorthosites of the three distinct regions captured three  
352 different intervals of geomagnetic field intensities during the  
353 emplacement and cooling of the Beaver River diabase sills  
354 ca. 1092 Ma. To contextualize the high paleointensity val-  
355 ues, we plot the regional mean values (Table. S3) based on  
356 specimen-level paleointensity results together with calculated  
357 paleointensity values at 22°N latitude based on the PADM2M  
358 model of the time-varying geomagnetic field over the past 2  
359 million years (38) in Figure 4B. The locality-mean values of  
360 these three regions are plotted in Figure 4C (and reported in  
361 Table. S3) where we also present the distribution of means  
362 calculated from 3 random values from the PADM2M model  
363 for a total of 10000 iterations. In addition, we perform the  
364 same comparison with the existing paleointensity data for  
365 the Cenozoic Era (the last 66 million years) from the PINT  
366 database (filtered by  $QPI \geq 3$ ; Fig. S5) given that the observa-  
367 tional dataset could record more geomagnetic field excursions  
368 or regional high flux patches. The anorthosite xenoliths 3  
369 region mean intensity is higher than all values from the re-  
370 sample results of the PADM2M model, and rival the top 3%  
371 values of the resample averages from the Cenozoic data (Fig.  
372 S5). These data supports that the anorthosite xenoliths likely  
373 record an exceptionally strong geomagnetic field ca. 1092 Ma.  
374

## Discussion

The crystallization of the solid inner core is an important event  
377 in the long-term evolution of Earth's core and in sustaining the  
378 geodynamo (1). The age of the inner core in thermal evolution  
379 models relies on estimates for the thermal conductivity of iron  
380 alloys at the temperatures and pressures of the core (53). Prior  
381 to studies in the last 10 years, an accepted value of  $\sim 30 \text{ W m}^{-1} \text{ K}^{-1}$  for this thermal conductivity was used to constrain  
382 the timing of inner core nucleation to be during the first half  
383 of Earth history (7, 54). Subsequently, experimental data and  
384 *ab initio* simulations were interpreted to imply higher thermal  
385 conductivity values (8, 14) which in turn imply a younger age  
386 of the inner core (<700 Ma; 13). However, other experimental  
387 studies continue to indicate lower thermal conductivity values  
388 consistent with prior estimates (7, 55) with no consensus  
389 yet emerging (53, 56). These experiments are challenging to  
390 conduct and interpret given complexities such as constraining  
391 the sample thickness under high pressure and temperature  
392 conditions, the validity of applying the Wiedemann-Franz law  
393 to extrapolate thermal conductivity values based on electrical  
394 resistivity measurements (14), and propagating uncertainties  
395 from free parameters used in finite element modeling of direct  
396

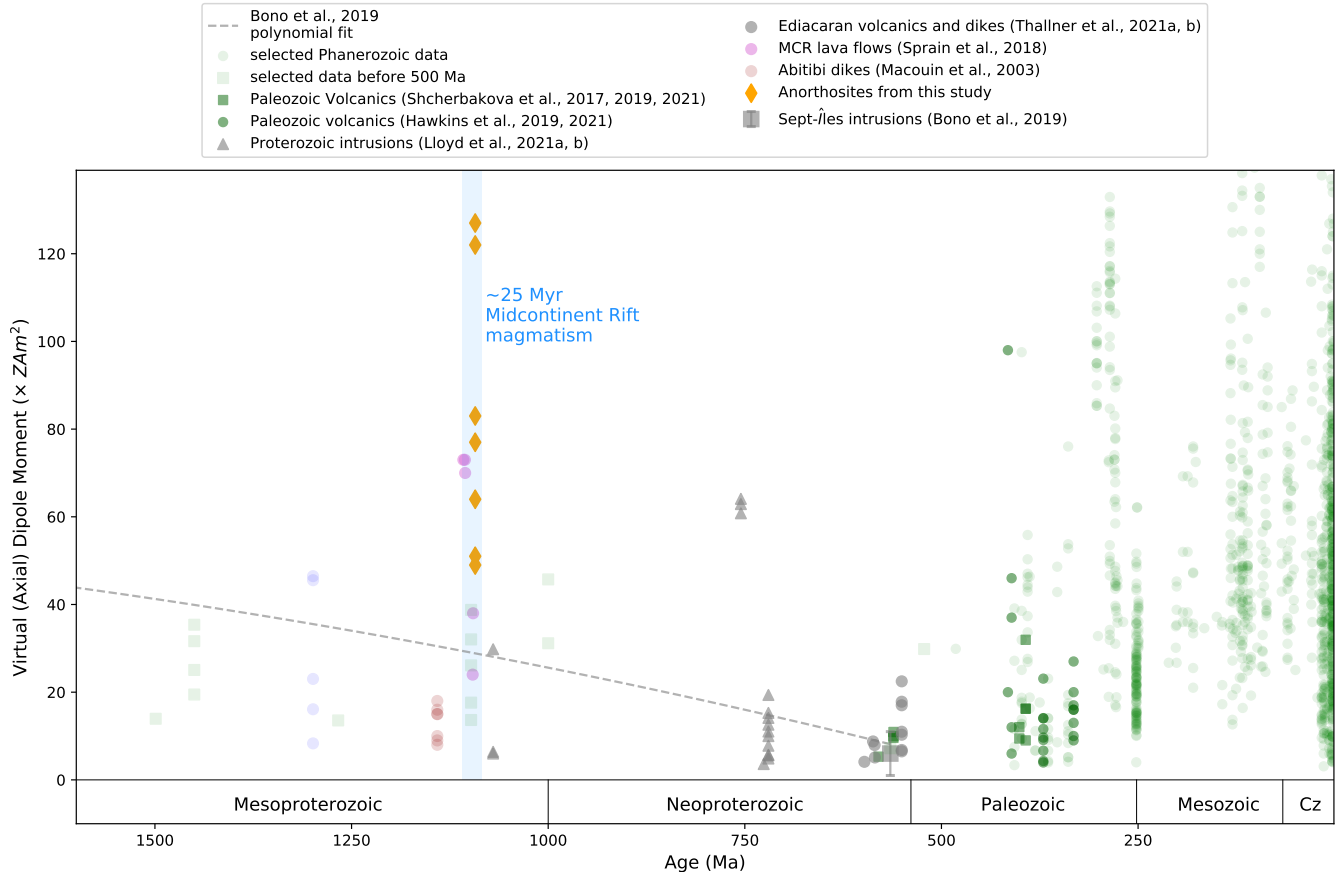


**Fig. 6.** Compilation of calculated virtual (axial) dipole moment values from the PINT database (PINT v8.0.0; <http://www.pintdb.org/>; 49), including all Phanerozoic VDM and VADM records with  $Q_{PI} > 3$  and additional Neoproterozoic data from refs. 18, 50–52. Paleointensity estimates from (22) and (23) are not included in the compilation due to the specimen-level double-slope behavior as discussed in the text. Overall the anorthosite xenoliths from this study record a high Mesoproterozoic field exceeding the value projected by the second order polynomial curve from (16) which is based on an interpretation of there being a monotonic decay of the geodynamo through the Proterozoic. The highest site-mean virtual dipole moment of the anorthosites would rank in the top 2% of those in the database for the Cenozoic Era (the last 66 million years) when there was unequivocally a crystallizing inner core. The y axis maximum is set at the 99 percentile of the compiled Cenozoic paleointensity data.

thermal conduction experiments (7). Further experiments and theory are needed to explain these contrasting results which at present leave open very different trajectories for Earth's thermal evolution. As a result, the age of the inner core is relatively unconstrained from a theoretical perspective.

The other data type that can provide insight into the long-term history of the core's thermal regime and geodynamo is paleomagnetic data—both paleodirectional data that indicate the presence of a geomagnetic field and paleointensity data that constrain the field's strength. Inner core nucleation would have increased the power to the geodynamo which has the potential to manifest as an increase in Earth's surface field (57). An approach combining dynamo simulations and theoretical scaling relationships has predicted that progressive decay of the field's dipole moment would be followed by a rapid increase in geomagnetic field intensity soon after the onset of inner core nucleation such that there is a minimum in dipole moment just before inner core nucleation (57). Other scenarios are possible, however, such as the model-based prediction that while power increases associated with inner core nucleation strengthen Earth's internal magnetic field, that the dynamo becomes more deeply seated in the core diminishes the increase in magnetic field strength at Earth's surface (58, 59). Such a scenario where the dynamo shifts to a greater depth associated with inner

core nucleation led (58) to conclude that the increase in power to the dynamo would be difficult to detect with paleointensity data. Ultimately, further observational paleomagnetic records is key as they hold the potential for testing different model predictions and identifying transitions in ancient field strength (16, 60).

It has been proposed that Proterozoic paleointensity data are consistent with a progressive monotonic decay leading up to ca. 565 Ma in the Ediacaran Period (Fig. 6; 16). This interpretation was motivated by paleointensity estimates developed from the ca. 565 Ma Sept-Îles layered mafic intrusive complex of  $\sim 7 \text{ ZAm}^2$  that are among the lowest values in the paleointensity database (Fig. 6; 16). A decay in the lead-up to this time was argued to be consistent with an absence of an inner core and a dynamo to which progressively less power was available through secular cooling (16, 57). This timing of inner core formation would favor a high core thermal conductivity (e.g. 14). Paleomagnetic directional excursions (61), other weak paleointensity estimates (18), and frequent polarity reversals (62) in rocks of similar age are interpreted to be consistent with numerical simulations (63) associated with a weak dipole field.

The high paleointensity estimates from the 1.1 billion-year-old Midcontinent Rift rocks challenge the hypothesized mono-

tonic decay of the strength of the geomagnetic field throughout the Proterozoic Era (Fig. 6). The well-preserved ca. 1092 Ma anorthosite xenoliths of the Beaver River diabase record a strong geomagnetic field in the late Mesoproterozoic that exceeds the strength of the modern-day field for which crystallization of the inner core is a power source (Figs. 4 and 6). Together with previous records obtained from the ca. 1106 Ma Osler Volcanics of the Midcontinent Rift (24), these data indicate that appreciable power to Earth's dynamo persisted through at least 14 Myr during the late Mesoproterozoic to maintain a strong surface field (Fig. 6). In addition to these high geomagnetic fields recorded by Midcontinent Rift rocks, the ca. 755 Ma Mundine Well dikes (51) also require a stronger geomagnetic field in the Neoproterozoic than would be predicted by a progressive Proterozoic decline (Fig. 6).

The hypothesis that a weak Ediacaran geomagnetic field is a telltale sign of the lack of an inner core with core nucleation following shortly thereafter may predict that it is the most significant weak to strong field transition in the paleointensity record. However, Fig. 6 shows that transitions from low to high field intensities occurred before, during, and after the Ediacaran Period. In the Ediacaran record developed to date, there is a two-fold increase in Earth's virtual dipole moment when comparing estimates from the ca. 565 Ma Sept-Îles intrusions (16) to those from ca. 550 Ma volcanics of the Skinner Cove Formation (52) (Fig. 6). In the late Mesoproterozoic, there is at least a six-fold increase within a period of ~35 Myr from a low average virtual dipole moment of ~13 ZAm<sup>2</sup> recorded by the ca. 1140 Ma Abitibi dikes which yielded straight Arai plots (64), to a high moment of ~70 ZAm<sup>2</sup> recorded by the ca. 1106 Ma Osler Volcanics, with even stronger values from ca. 1092 Ma by Beaver River anorthosite xenoliths that record virtual dipole moments up to ~127 ZAm<sup>2</sup>. While the ca. 1140 Abitibi dikes paleointensity estimates do not go to values as low as the ca. 565 Ma Sept-Îles intrusions, this virtual dipole moment increase in the Mesoproterozoic from the ca. 1140 Ma data to the ca. 1100 Ma data is the largest yet documented in the Precambrian on a 10s of millions of years timescale (Fig. 6). The tempo and scale of this field intensity transition could match with model-based predictions associated with the onset of inner core nucleation (57). This ca. 1.1 Ga timing would be broadly consistent with the ca. 1.3 Ga onset proposed by ref. 60 albeit later given the exclusion of previous overestimated paleointensity values from the ca. 1.3 Ga Gardar basalts that are superseded by data in ref. 65. However, a model prediction of sustained strong field values following inner core nucleation is challenged by data from the ca. 1070 Ma Bangemann Sills which include a sill with a low virtual dipole moment of ~6.4 ZAm<sup>2</sup> (Fig. 6; 51). Following the Ediacaran, there are also low paleointensity estimates from Devonian rocks such as ca. 370 Ma dikes and lavas of the Siberian Viluy Traps that give virtual dipole moment estimates of 4.3 to 14.9 ZAm<sup>2</sup> (Fig. 6; 66). These low values as well as data from the ca. 414 Ma Strathmore lava flows (21), the ca. 410–380 Ma lava flows of Siberia and the Kola Peninsula (19), the ca. 408–393 Ma Burabay volcanics (20) and the ca. 332 Ma Kinghorn volcanics (21) has led to the proposal of this interval as the "Mid-Paleozoic Dipole Low" (21). This "Mid-Paleozoic Dipole Low" is followed by high paleointensity values such that there is a six-fold increase in the database from virtual dipole moment of ~16 ZAm<sup>2</sup> at ca. 332 Ma to

~99 ZAm<sup>2</sup> ca. 308 Ma in the late Carboniferous (Fig. 6; 21). Given that the multiple records of a weak field in the Proterozoic and Paleozoic cannot all be the minimum prior to the singular event of the onset of inner core nucleation, what processes could lead to a weak dipole at Earth's surface even in the presence of a crystallizing inner core? Numerical models have shown that the dipole moment is sensitive to both the magnitude and spatial pattern of heat flow across the core-mantle boundary when there are strong available power sources to the geodynamo (67, 68). In such models, relatively low total heat flux across the core-mantle boundary can prevent the axial dipole from reversing whereas a high heat flux through the boundary can result in an increase in reversal frequency and decrease in dipole intensity. The "Mid-Paleozoic Dipole Low" has been hypothesized to be the result of such elevated core-mantle boundary heat flux conditions at a time when there was also available power from a crystallizing inner core (66), thereby also explaining the observed low paleointensities which include values as weak as those of the ca. 565 Ma Sept-Îles intrusions (Fig. 6; 16). Mantle convection can modulate core mantle boundary heat flow through changes in the structure of the deep mantle associated with upwelling plumes (69, 70) and subducted slabs (71–73). Strong evidence for differential plate tectonic motion extends back to ca. 2.2 Ga in the Paleoproterozoic (74, 75) and potentially back to ca. 3.2 Ga in the Archean (4). Plate tectonic modulations of core mantle boundary heat flow are therefore expected throughout the Proterozoic. Such changes may explain large variability in Proterozoic paleointensity values similar to those seen in the Phanerozoic (50) and may challenge our ability to detect the increase in surface geomagnetic field strength predicted to have happened at the onset of inner core crystallization.

Overall, the high-fidelity paleointensity recorders of the Beaver River anorthosite xenoliths in the well-preserved Mid-continent Rift record strong field strengths 1.1 billion years ago. The highest site-level value of the virtual dipole moment would rank in the top 2% of those in the database for the Cenozoic Era when there was unequivocally a crystallizing inner core. These high surface field strengths necessitate appreciable power to the late Mesoproterozoic geodynamo.

## Materials and Methods

**Sample collection and paleomagnetic directions.** We collected paleomagnetic cores that are 2.5 cm in diameter along the southern and eastern Beaver Bay Complex with a particular focus on acquiring paired sites of anorthosite xenoliths and their local diabase hosts during summer field seasons in 2019 and 2020. Sample cores were collected using a hand-held gasoline-powered drill and were oriented using a magnetic compass as well as a sun compass when possible. Sun compass orientations were preferentially used for determining the sample azimuth. Sister specimens underwent step-wise alternating field (AF) or thermal demagnetization at the UC Berkeley Paleomagnetism Lab to isolate paleomagnetic directions (data presented in 30). Based on the anorthosite thermal demagnetization results, we selected sites whose unblocking temperature ranges are narrow and near 580°C for paleointensity experiments. Beaver River diabase sites with minimal secondary remanence were also selected for paleointensity experiments.

**Paleointensity experiment.** A total of 86 specimens from 14 anorthosite xenoliths and a total of 69 specimens from 7 diabase sites underwent paleointensity experiments that followed the step-wise double-heating Thellier method (76) using the IZZI protocol (27)

with heating steps up to 585 °C. Partial thermal remanent magnetization (pTRM) checks were performed systematically throughout the experiment to test whether there was significant mineralogical alteration due to heating and were assessed using the SCAT parameter of 77. On top of the IZZI-Thellier experiment protocol, we also performed a comparative study where we added an extra step of 20 mT alternating field (AF) cleaning on some of the specimens after each in-field step. The purpose is to study whether the AF cleaning could help improve experiment success rate by removing the remanence component carried by materials such as multi-domain (MD) grains that contribute to non-ideal paleointensity behaviors. The results were similar when this step was applied without an observed change in experimental success rate. All remanence measurements were made on a 2G Enterprises DC-SQUID superconducting rock magnetometer equipped with an automated sample changer system at the UC Berkeley Paleomagnetism laboratory. The magnetometer is housed inside a three-layer magnetostatic shield that maintains background fields of less than 500 nT. Heating steps were performed using an ASC TD-48SC thermal demagnetizer with a controlled field coil that allows for a magnetic field to be generated in the oven in conjunction with a DC power supply. The thermal demagnetizer was degassed with an alternating field in the axial orientation following each in-field step such that residual fields within the oven were <10 nT during zero-field steps. Samples were placed in the same location within the thermal demagnetizer for each heating step and were maintained in the same orientation with regard to the applied field. During each heating step, the oven remained at peak temperatures for 20 min to make sure each specimen reached the target temperature. An applied laboratory field of 30  $\mu$ T was used for all in-field steps. All heating steps were performed in air. The temperature increments for the experiments were chosen to isolate magnetizations held by (titano)magnetite informed by the previous demagnetization data, with smaller increments performed close to the expected unblocking temperature of ~580°C.

**Paleointensity result selection.** The following criteria were used as quality filters on the paleointensity results: (1) a maximum angular deviation (MAD; 78) of <20°; (2) scatter parameter ( $\beta$ ; 79) values of <15%; (3) a deviation angle (DANG; 80) of <5°; (4) fraction of remanence fitted for paleointensity estimate (FRAC; (77)) >0.6; (5) scatter statistic (SCAT; 77) = TRUE; (6) a maximum magnetic moment difference between adjacent zero-field steps (GAP-Max; 77) < 0.25; (7) number of pTRM checks > 2; (8) and number of measurements used for paleointensity determination  $\geq$  4. The MAD measures the scatter about the best-fit line through the natural remanent magnetization (NRM) steps in the selected interval for which the intensity is defined. DANG, the deviation angle, is the angle between the best-fit direction that is free floating and the direction between the centre of mass of the data and the origin of the vector component diagram (80). Both MAD and DANG assess the directional variation of the NRM, with MAD measuring the scatter in the NRM directions and DANG assessing whether the component is trending toward the origin of the Zijderveld plot.  $\beta$  is the “scatter” parameter of (79) and is the ratio of the standard error of the slope of the best-fit line of the selected NRM and pTRM points on an NRM/TRM plot to the absolute value of the slope. FRAC is the fraction of the NRM that is used in the best-fit line (77). The FRAC value was chosen to preferentially select samples with dominantly single-slope NRM/TRM plots. GAP-Max is the maximum gap between two points on the NRM/TRM plot determined by vector arithmetic. SCAT is a Boolean operator which uses the error on the best-fit slope of the selected data on the NRM/TRM plot to determine if the data are overly scattered. The parameter is used to assess pTRM checks in addition to assessing the degree to which IZZI steps are zigzagged.  $\beta$ , FRAC, GAP-Max and SCAT are all statistics to assess the behavior of NRM/TRM plots. See the Standard Paleointensity Definitions (81; <https://earthorg/PmagPy/SPD/home.html>) for more details. Data analysis was conducted using Thellier GUI (77) within the PmagPy software package (37).

**Rock magnetic experiments.** We conducted rock magnetic experiments with a purpose of gaining magnetic mineralogy insights into the paleointensity results of the anorthosite and diabase. Backfield curves were measured at room temperature using a Micromag Princeton Measurements vibrating sample magnetometer (VSM)

and a Lake Shore 8600 series VSM at the Institute for Rock Magnetism. Specimen median destructive fields (MDF) are calculated based on the backfield curves. The calculated coercivity spectra were subsequently decomposed into one or more components using skew-normal distributions following the method of 44 examples of which are shown in Fig. 5. We also used a magnetic property measurement system (MPMS) at the Institute for Rock Magnetism to aid in the identification of magnetic minerals. In the field-cooled (FC) experiments, specimen magnetizations were measured upon warming following the specimen having cooled in an applied field of 2.5 T from 300 to 10 K. In the zero-field-cooled (ZFC) experiment, a low-temperature saturation isothermal remanence (LTSIRM) of 2.5 T was applied at 10 K after the specimen cooled in a (near-)zero field. In the room-temperature saturation isothermal remanence (RTSIRM) experiment, the sample was pulsed with a 2.5 T field at room temperature (~300 K) and then cooled to 10 K and warmed back to room temperature in a (near-)zero field. The magnetic moment transitions at critical temperatures revealed through MPMS experiments are used to identify magnetic minerals such as magnetite within specimens (42).

To further identify the magnetic carriers within the Beaver River anorthosites xenoliths and compare them with the anorthosites of the Duluth Complex Anorthositic Series rocks, we used the quantum diamond microscope (QDM) at the UC Berkeley Paleomagnetism laboratory to image a thin section of sample MS99033 from anorthosite xenolith AX16 (which yielded a  $^{206}\text{Pb}/^{238}\text{U}$  zircon date of  $1091.83 \pm 0.21$  Ma; 30), and a thin section of a Duluth Complex anorthosite (Fig. 2). We use the QDM to image the magnetic field over the polished thin section surfaces with a sample-sensor distance of 5  $\mu\text{m}$  in projective magnetic microscopy (PMM) mode with a spatial resolution of 4.7 m per pixel and an instantaneous 0.9 mT bias field that is canceled during the course of measurement (82).

**ACKNOWLEDGMENTS.** Project research was supported by NSF CAREER grant EAR-1847277 to N.L.S.-H., an Institute on Lake Superior Geology Student Research Fund grant to Y.Z., and an Institute for Rock Magnetism Visiting Student Fellowship to Y.Z. The Institute for Rock Magnetism is supported by the Instrumentation and Facilities program of the NSF Earth Science Division. Permits for fieldwork and sampling from the Minnesota Department of Natural Resources are gratefully acknowledged. We thank James Pierce and Blake Hodgin for their assistance in the field. We thank Jim Miller for providing us with the Duluth Complex anorthosite thin section. We thank Dario Bilardello, Peat Solheid, Mike Jackson, Josh Feinberg, and Bruce Moskowitz for their tremendous help associated with instrument operation, data interpretations, and research guidance at the IRM. Conversations with Bruce Buffett and Zachary Geballe informed our perspectives on the geodynamic and mineral physics literature. Paleomagnetic data associated with this study are available within the MagIC database (<https://earthorg/MagIC/19462-8d3c2258-11ae-4830-b99f-3f6b02cecb7e; provide link when doi is generated at time of proofs>) and all data are within a Github repository along with Python code related to calculations and visualizations ([https://github.com/Swanson-Hysell-Group/AX\\_BD\\_PINT](https://github.com/Swanson-Hysell-Group/AX_BD_PINT)) that are also archived on Zenodo (*provide link when doi is generated at time of proofs*).

1. BA Buffett, Earth's core and the geodynamo. *Science* **288**, 2007–2012 (2000).
2. P Selkin, J Gee, L Tauxe, Nonlinear thermoremanence acquisition and implications for paleointensity data. *Earth Planet. Sci. Lett.* **256**, 81–89 (2007).
3. JA Tarduno, EG Blackman, EE Mamajek, Detecting the oldest geodynamo and attendant shielding from the solar wind: Implications for habitability. *Phys. Earth Planets. Interiors* **233**, 68–87 (2014).
4. AR Brenner, et al., Paleomagnetic evidence for modern-like plate motion velocities at 3.2 Ga. *Sci. Adv.* **6**, eaaz8670 (2020).
5. CJ Davies, M Pozzo, D Gubbins, D Alfè, Constraints from material properties on the dynamics and evolution of Earth's core. *8*, 678–685 (2015).
6. D Gubbins, D Alfè, G Masters, GD Price, M Gillan, Gross thermodynamics of two-component core convection. *Geophys. J. Int.* **157**, 1407–1414 (2004).
7. Z Konopková, RS McWilliams, N Gómez-Pérez, AF Goncharov, Direct measurement of thermal conductivity in solid iron at planetary core conditions. *Nature* **534**, 99–101 (2016).
8. M Pozzo, C Davies, D Gubbins, D Alfè, Thermal and electrical conductivity of iron at Earth's core conditions. *Nature* **485**, 355–358 (2012).

9. N de Koker, G Steinle-Neumann, V Vlcek, Electrical resistivity and thermal conductivity of liquid Fe alloys at high P and T, and heat flux in Earth's core. *Phys. Earth Planet. Interiors* **109**, 4070–4073 (2012).
10. H Gomi, et al., The high conductivity of iron and thermal evolution of the Earth's core. *Phys. Earth Planet. Interiors* **224**, 88–103 (2013).
11. Y Zhang, et al., Reconciliation of experiments and theory on transport properties of iron and the geodynamo. *Nature* **125** (2020).
12. DA Frost, et al., Multidisciplinary constraints on the thermal-chemical boundary between Earth's core and mantle. *Geochem. Geophys. Geosystems* (2022).
13. S Labrosse, Thermal evolution of the core with a high thermal conductivity. *Phys. Earth Planet. Interiors* **247**, 36–55 (2015).
14. K Ohta, Y Kuwayama, K Hirose, K Shimizu, Y Ohishi, Experimental determination of the electrical resistivity of iron at Earth's core conditions. *Nature* **534**, 95–98 (2016).
15. NL Swanson-Hysell, The Precambrian paleogeography of Laurentia in *Ancient Supercontinents and the Paleogeography of Earth*. (Elsevier), pp. 109–153 (2021).
16. RK Bono, JA Tarduno, F Nimmo, RD Cotterell, Young inner core inferred from Ediacaran ultra-low geomagnetic field intensity. *Nat. Geosci.* **12**, 143–147 (2019).
17. VV Shcherbakova, et al., Ultra-low paleointensities from East European Craton, Ukraine support a globally anomalous palaeomagnetic field in the Ediacaran. *Geophys. J. Int.* **220**, 1928–1946 (2019).
18. D Thallner, AJ Biggin, HC Halls, An extended period of extremely weak geomagnetic field suggested by paleointensities from the Ediacaran Grenville dykes (SE Canada). *Earth Planet. Sci. Lett.* **568**, 117025 (2021).
19. VV Shcherbakova, et al., Was the Devonian geomagnetic field dipolar or multipolar? Palaeointensity studies of Devonian igneous rocks from the Minusa Basin (Siberia) and the Kola Peninsula dykes, Russia. *Geophys. J. Int.* **209**, 1265–1286 (2017).
20. VV Shcherbakova, et al., Ultra-Low Geomagnetic Field Intensity in the Devonian Obtained from the Southern Ural Rock Studies. *Izvestiya, Phys. Solid Earth* **57**, 900–912 (2021).
21. LMA Hawkins, et al., Intensity of the Earth's magnetic field: Evidence for a Mid-Paleozoic dipole low. *Proc. Natl. Acad. Sci.* **118**, e2017342118 (2021).
22. LJ Pesonen, HC Halls, Geomagnetic field intensity and reversal asymmetry in late Precambrian Keweenawan rocks. *Geophys. J. Int.* **73**, 241–270 (1983).
23. EV Kulakov, AV Smirnov, JF Diehl, Absolute geomagnetic paleointensity as recorded by ~1.09 Ga Lake Shore Traps (Keweenaw Peninsula, Michigan). *Studia Geophys. et Geod.* **57**, 565–584 (2013).
24. CJ Sprain, NL Swanson-Hysell, LM Fairchild, K Gaaster, A field like today's? The strength of the geomagnetic field 1.1 billion years ago. *Geophys. J. Int.* **213**, 1969–1983 (2018).
25. J Kasbohm, B Schoene, S Burgess, Radiometric constraints on the timing, tempo, and effects of large igneous province emplacement (2021).
26. NL Swanson-Hysell, et al., Rapid emplacement of massive Duluth Complex intrusions within the North American Midcontinent Rift. *Geology* (2021).
27. Y Yu, L Tauxe, A Genevey, Toward an optimal geomagnetic field intensity determination technique. *Geochem. Geophys. Geosystems* **5** (2004).
28. DJ Dunlop, Ö Özdemir, Beyond Néel's theories: thermal demagnetization of narrow-band partial thermoremanent magnetizations. *Phys. Earth Planet. Interiors* **126**, 43–57 (2001).
29. L Tauxe, et al., Understanding Nonideal Paleointensity Recording in Igneous Rocks: Insights From Aging Experiments on Lava Samples and the Causes and Consequences of "Fragile" Curvature in Arai Plots. *Geochem. Geophys. Geosystems* **22** (2020).
30. Y Zhang, NL Swanson-Hysell, MD Schmitz, JD Miller, MS Avery, Synchronous emplacement of the anorthosite xenolith-bearing Beaver River diabase and one of the largest lava flows on Earth. *Geochem. Geophys. Geosystems* (2021).
31. NL Swanson-Hysell, J Ramezani, LM Fairchild, IR Rose, Failed rifting and fast drifting: Mid-continent Rift development, Laurentia's rapid motion and the driver of Grenvillian orogenesis. *GSA Bull.* **131**, 913–940 (2019).
32. TJ Boerboom, M-147 Bedrock geology of the Split Rock Point quadrangle, Lake County, Minnesota, (Minnesota Geological Survey), Technical report (2004).
33. TJ Boerboom, JC Green, P Albers, J Miller, J.D., M-171 Bedrock geology of the Tofte quadrangle, Cook County, Minnesota, (Minnesota Geological Survey), Technical report (2006).
34. JM Feinberg, HR Wenk, GR Scott, PR Renne, Preferred orientation and anisotropy of seismic and magnetic properties in gabbroites from the Bushveld layered intrusion. *Tectonophysics* **420**, 345–356 (2006).
35. P Selkin, J Gee, L Tauxe, W Meurer, A Newell, The effect of remanence anisotropy on paleointensity estimates: a case study from the Archean Stillwater Complex. *Earth Planet. Sci. Lett.* **183**, 403–416 (2000).
36. AJ Biggin, GA Paterson, A new set of qualitative reliability criteria to aid inferences on palaeomagnetic dipole moment variations through geological time. *Front. Earth Sci.* **2** (2014).
37. L Tauxe, et al., PmagPy: Software package for paleomagnetic data analysis and a bridge to the Magnetics Information Consortium (MagIC) Database. *Geochem. Geophys. Geosystems* **17**, 2450–2463 (2016).
38. LB Ziegler, CG Constable, CL Johnson, L Tauxe, PADM2m: a penalized maximum likelihood model of the 0–2 ma palaeomagnetic axial dipole moment. *Geophys. J. Int.* **184**, 1069–1089 (2011).
39. B Cych, M Morzfeld, L Tauxe, Bias corrected estimation of paleointensity (BiCEP): An improved methodology for obtaining paleointensity estimates. *Geochem. Geophys. Geosystems* **22** (2021).
40. GA Paterson, A simple test for the presence of multidomain behavior during paleointensity experiments. *J. Geophys. Res.* **116** (2011).
41. EJW Verwey, Electronic Conduction of Magnetite ( $\text{Fe}_3\text{O}_4$ ) and its Transition Point at Low Temperatures. *Nature* **144**, 327–328 (1939).
42. JM Feinberg, PA Solheid, NL Swanson-Hysell, MJ Jackson, JA Bowles, Full vector low-temperature magnetic measurements of geologic materials. *Geochem. Geophys. Geosystems* **16**, 301–314 (2015).
43. Ö Özdemir, DJ Dunlop, BM Moskowitz, The effect of oxidation on the Verwey transition in magnetite. *Geophys. Res. Lett.* **20**, 1671–1674 (1993).
44. DP Maxbauer, JM Feinberg, DL Fox, MAX UnMix: A web application for unmixing magnetic coercivity distributions. *Comput. Geosci.* **95**, 140–145 (2016).
45. S Xu, DJ Dunlop, Thellier paleointensity theory and experiments for multidomain grains. *J. Geophys. Res. Solid Earth* **109** (2004).
46. MH Dodson, E McClelland-Brown, Magnetic blocking temperatures of single-domain grains during slow cooling. *J. Geophys. Res.* **85**, 2625 (1980).
47. SL Halgedahl, R Day, M Fuller, The effect of cooling rate on the intensity of weak-field trm in single-domain magnetite. *J. Geophys. Res. Solid Earth* **85**, 3690–3698 (1980).
48. L Nagy, W Williams, L Tauxe, Estimating the effect of cooling rate on the acquisition of magnetic remanence. *Geophys. Res. Lett.* **48** (2021).
49. RK Bono, et al., The PINT database: A definitive compilation of absolute palaeomagnetic intensity determinations since 4 billion years ago. *Geophys. J. Int.* (2021).
50. SJ Lloyd, AJ Biggin, H Halls, MJ Hill, First Palaeointensity Data from the Cryogenian and their potential implications for Inner Core Nucleation Age. *Geophys. J. Int.* (2021).
51. SJ Lloyd, AJ Biggin, ZX Li, New paleointensity data suggest possible Phanerozoic-type paleomagnetic variations in the Precambrian. *Geochem. Geophys. Geosystems* (2021).
52. D Thallner, AJ Biggin, PJA McCausland, RR Fu, New paleointensities from the Skinner Cove Formation, Newfoundland, suggest a changing state of the geomagnetic field at the Ediacaran-Cambrian transition. *J. Geophys. Res. Solid Earth* (2021).
53. K Ohta, K Hirose, The thermal conductivity of the Earth's core and implications for its thermal and compositional evolution. *Natl. Sci. Rev.* **8** (2021).
54. F Stacey, D Loper, A revised estimate of the conductivity of iron alloy at high pressure and implications for the core energy balance. *Phys. Earth Planet. Interiors* **161**, 13–18 (2007).
55. WP Hsieh, et al., Low thermal conductivity of iron-silicon alloys at Earth's core conditions with implications for the geodynamo. *Nat. Commun.* **11** (2020).
56. Q Williams, The thermal conductivity of Earth's core: a key geophysical parameter's constraints and uncertainties. *Annu. Rev. Earth Planet. Sci.* **46**, 47–66 (2018).
57. CJ Davies, et al., Dynamo constraints on the long-term evolution of Earth's magnetic field strength. *Geophys. J. Int.* (2021).
58. J Albert, Stéphane, C Poitou, Modelling the palaeo-evolution of the geodynamo. *Geophys. J. Int.* **179**, 1414–1428 (2009).
59. M Landeau, J Albert, P Olson, The signature of inner-core nucleation on the geodynamo. *Earth Planet. Sci. Lett.* **465**, 193–204 (2017).
60. AJ Biggin, et al., Palaeomagnetic field intensity variations suggest Mesoproterozoic inner-core nucleation. *Nature* **526**, 245–248 (2015).
61. HC Halls, A Lovette, M Hamilton, U Söderlund, A paleomagnetic and U–Pb geochronology study of the western end of the Grenville dyke swarm: Rapid changes in paleomagnetic field direction at ca. 585Ma related to polarity reversals? *Precambrian Res.* **257**, 137–166 (2015).
62. KP Kodama, Combined magnetostratigraphy from three localities of the Rainstorm Member of the Johnnie Formation in California and Nevada, United States Calibrated by Cyclostratigraphy: A 13 R/Ma Reversal Frequency for the Ediacaran. *Front. Earth Sci.* **9** (2021).
63. PE Driscoll, Simulating 2 Ga of geodynamo history. *Geophys. Res. Lett.* **43**, 5680–5687 (2016).
64. M Macoun, et al., Low paleointensities recorded in 1 to 2.4 Ga Proterozoic dykes, Superior Province, Canada. *Earth Planet. Sci. Lett.* **213**, 79–95 (2003).
65. KP Kodama, LK Carnes, JA Tarduno, C Bertti, Palaeointensity of the 1.3 billion-yr-old Gardar basalts, southern Greenland revisited: no evidence for onset of inner core growth. *Geophys. J. Int.* **217**, 1974–1987 (2019).
66. L Hawkins, et al., An exceptionally weak Devonian geomagnetic field recorded by the Viluy Traps, Siberia. *Earth Planet. Sci. Lett.* **506**, 134–145 (2019).
67. P Olson, Gravitational dynamos and the low-frequency geomagnetic secular variation. *Proc. Natl. Acad. Sci.* **104**, 20159–20166 (2007).
68. PL Olson, RS Coe, PE Driscoll, GA Glatzmaier, PH Roberts, Geodynamo reversal frequency and heterogeneous core–mantle boundary heat flow. *Phys. Earth Planet. Interiors* **180**, 66–79 (2010).
69. RL Larson, P Olson, Mantle plumes control magnetic reversal frequency. *Earth Planet. Sci. Lett.* **107**, 437–447 (1991).
70. V Courtillot, P Olson, Mantle plumes link magnetic superchrons to Phanerozoic mass depletion events. *Earth Planet. Sci. Lett.* **260**, 495–504 (2007).
71. E Tan, M Gurnis, L Han, Slabs in the lower mantle and their modulation of plume formation. *Geochem. Geophys. Geosystems* **3**, 1–24 (2002).
72. AJ Biggin, et al., Possible links between long-term geomagnetic variations and whole-mantle convection processes. *Nat. Geosci.* **5**, 526–533 (2012).
73. MW Hounslow, M Domier, AJ Biggin, Subduction flux modulates the geomagnetic polarity reversal rate. *Tectonophysics* **742–743**, 34–49 (2018).
74. RN Mitchell, et al., Plate tectonics before 2.0 Ga: Evidence from paleomagnetism of cratons within supercontinent Nuna. *Am. J. Sci.* **314**, 878–894 (2014).
75. NL Swanson-Hysell, et al., The paleogeography of Laurentia in its early years: new constraints from the paleoproterozoic east-central Minnesota batholith. *Tectonics* (2021).
76. O Thellier, E; Thellier, Sur l'intensité du champ magnétique terrestre dans le passé historique et géologique. *Annales de Géophys.* **15**, 285–378 (1959).
77. R Shaar, L Tauxe, Thellier GUI: An integrated tool for analyzing paleointensity data from Thellier-type experiments. *Geochem. Geophys. Geosystems* **14**, 677–692 (2013).
78. JL Kirschvink, The least-squares line and plane and the analysis of palaeomagnetic data. *Geophys. J. Int.* **62**, 699–718 (1980).
79. RS Coe, S Grommé, EA Mankinen, Geomagnetic paleointensities from radiocarbon-dated lava flows on Hawaii and the question of the Pacific nondipole low. *J. Geophys. Res. Solid Earth* **83**, 1740–1756 (1978).
80. L Tauxe, H Staudigel, Strength of the geomagnetic field in the Cretaceous Normal Superchron: New data from submarine basaltic glass of the Troodos Ophiolite. *Geochem. Geophys. Geosystems* **5** (2004).
81. GA Paterson, L Tauxe, AJ Biggin, R Shaar, LC Jonestrask, On improving the selection of Thellier-type paleointensity data. *Geochem. Geophys. Geosystems* **15**, 1180–1192 (2014).
82. DR Glenn, et al., Micrometer-scale magnetic imaging of geological samples using a quantum diamond microscope. *Geochem. Geophys. Geosystems* **18**, 3254–3267 (2017).

1

2 **Supplementary Information for**

3 **High geomagnetic field intensity recorded by anorthosite xenoliths requires a vigorous late**  
4 **Mesoproterozoic geodynamo**

5 **Yiming Zhang, Nicholas L. Swanson-Hysell, Margaret S. Avery, Roger R. Fu**

6 **Yiming Zhang**

7 **E-mail: yimingzhang@berkeley.edu**

8 **This PDF file includes:**

9 Figs. S1 to S5

10 Tables S1 to S3

11 SI References

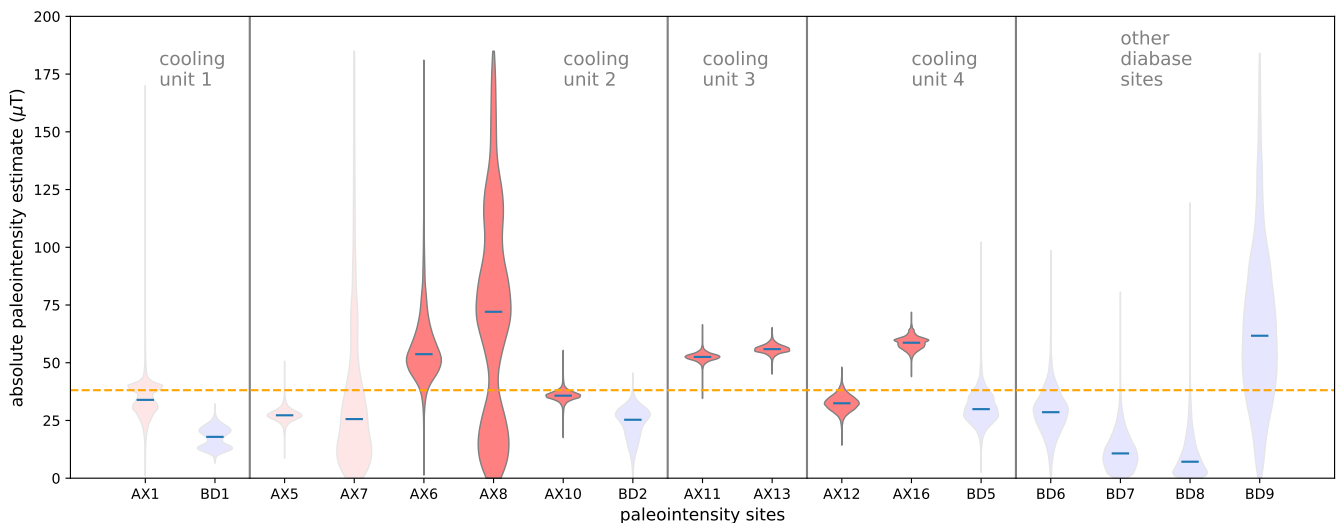


**Fig. S1.** Violin plots of site-level posterior paleointensity distributions estimated using the bias corrected estimation of paleointensity (BiCEP) method developed by 1. Assuming that paleointensity estimates from specimens that come from a same cooling unit are distributed around a true paleointensity value with the various deflections being expressed as the curvature parameter of the NRM/TRM plot (2, 3), the method uses all paleointensity measurement-level data without applying selection criteria. For comparison of results from this independent method with those based on our selection (as shown in Fig. 4 in manuscript), we highlight the anorthositic sites that pass our paleointensity selection and make other anorthositic and diabase transparent. The results from the BiCEP method address the uncertainties associated with anorthositic AX6 and AX8. This is associated with the relatively variable specimen behaviors within these two sites. But for sites AX10, AX11, AX13, AX12, and AX16, the posterior probability distributions have very narrow bounds, consistent with the interpretation that these anorthositic are faithful paleointensity recorders that have high-quality paleointensity behaviors.

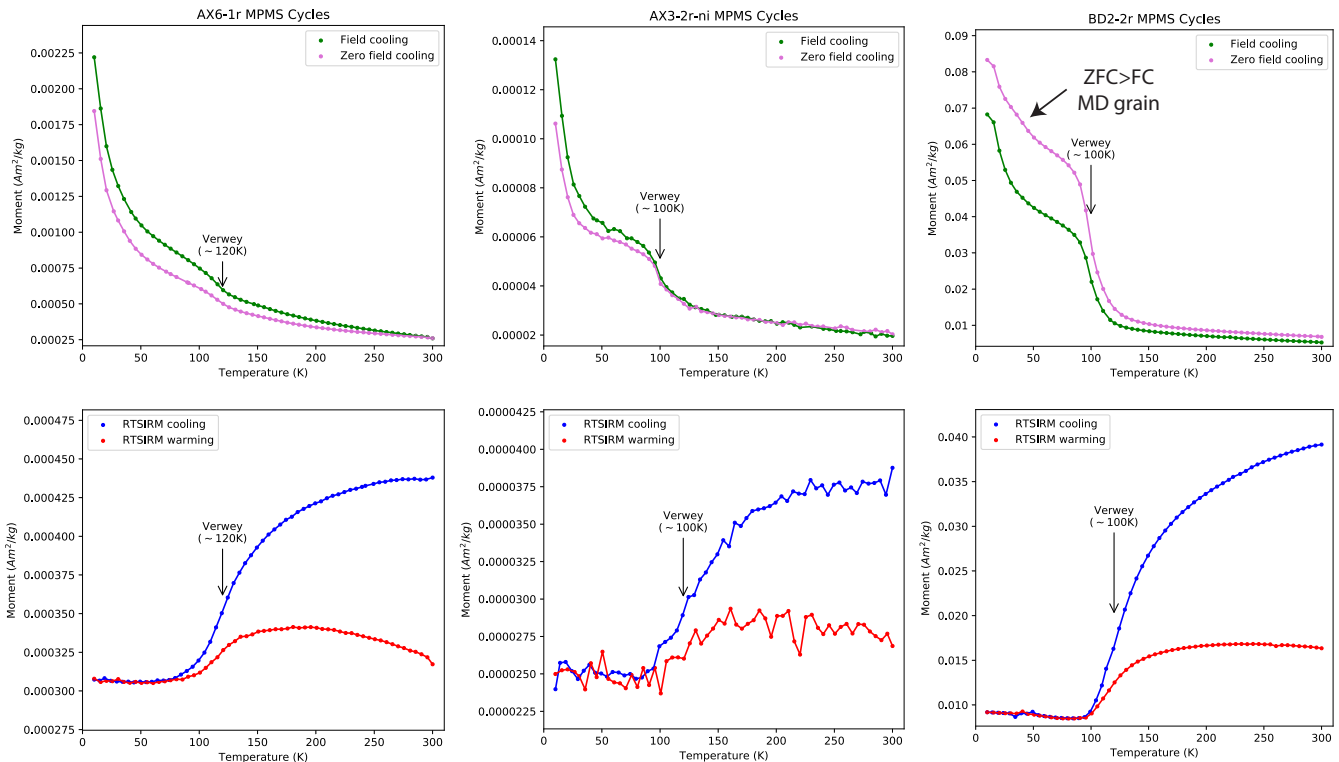


**Fig. S2.** Low-temperature magnetic property measurement system (MPMS) experiment results. In the field-cooled (FC) experiments, the magnetization was measured upon warming following the specimen having cooled in an applied field of 2.5 T from 300 to 10 K. In the zero-field-cooled (ZFC) experiment, a low-temperature saturation isothermal remanence (LTSIRM) of 2.5 T was applied at 10 K after the specimen cooled in a (near-)zero field. In the room-temperature saturation isothermal remanence (RTSIRM) experiment, the sample was pulsed with a 2.5 T field at room temperature ( $\sim 300$  K) and then cooled to 10 K and warmed back to room temperature in a (near-) zero field. Specimen AX6-1r is from anorthosite AX6 which passed our paleointensity selection. It has a well-defined Verwey transition  $\sim 120$  K (4). Specimens AX3-2r-ni and BD2-2r show Verwey transition but the transition temperatures are suppressed below  $\sim 120$  K. Specimen BD2-2r has a consistently higher moment during the zero-field-cooled step than during the field-cooled step. This is consistent with the interpretation that multidomian magnetic carriers exist in significant quantity in this specimen.

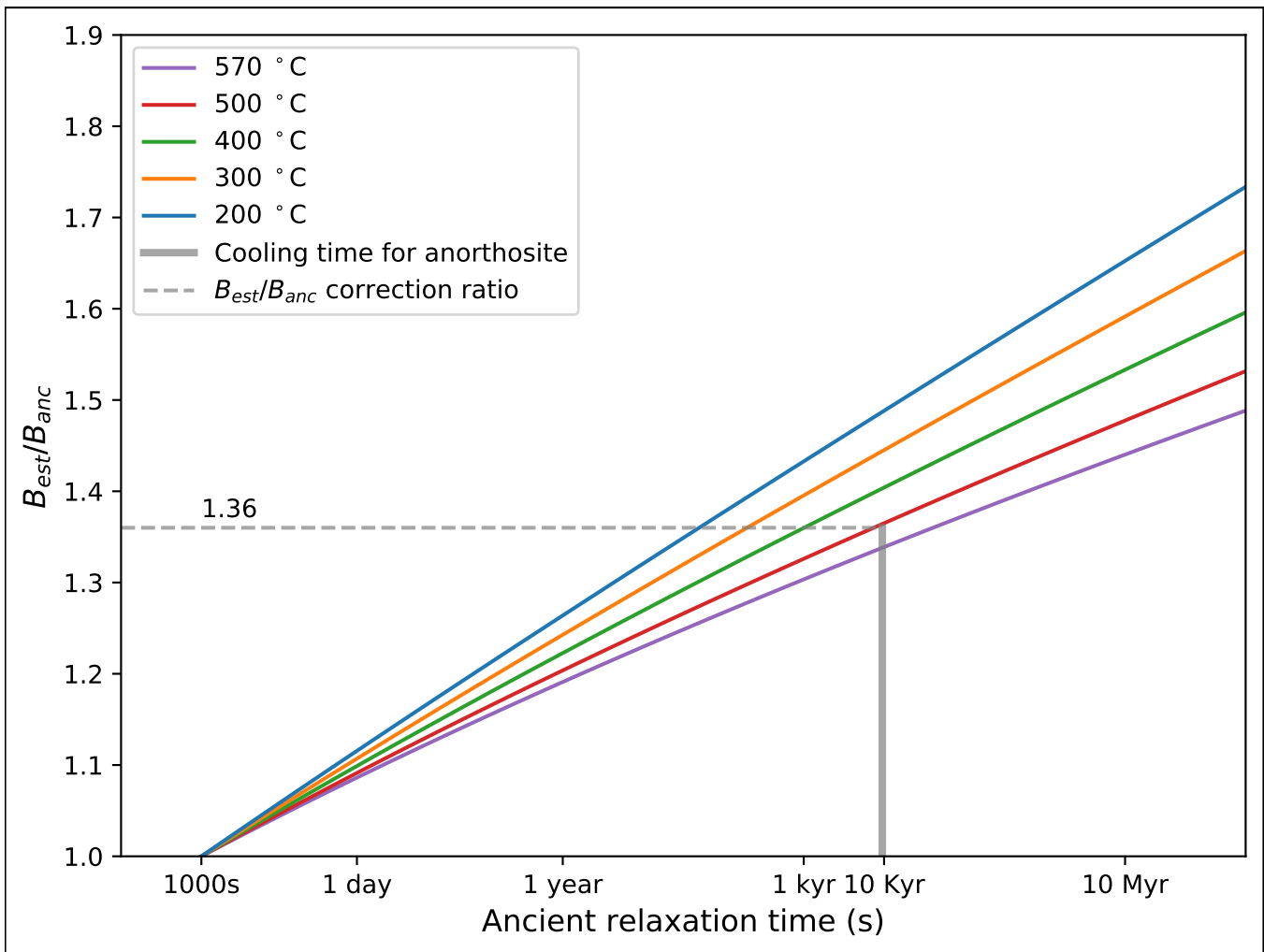


**Fig. S3.** Graph of predicted paleointensity overestimate due to slow cooling of the intrusive Beaver River diabase and anorthosite xenoliths relative to the cooling rate in laboratory following the model of 5. Because the majority of the anorthosites have unblocking temperatures between 500°C and 580°C, we estimate that the slow cooling during natural remanence acquisition could have resulted in a 36% overestimate. Thus, a correction factor of 0.74 is applied at specimen level for the paleointensity summary plot.

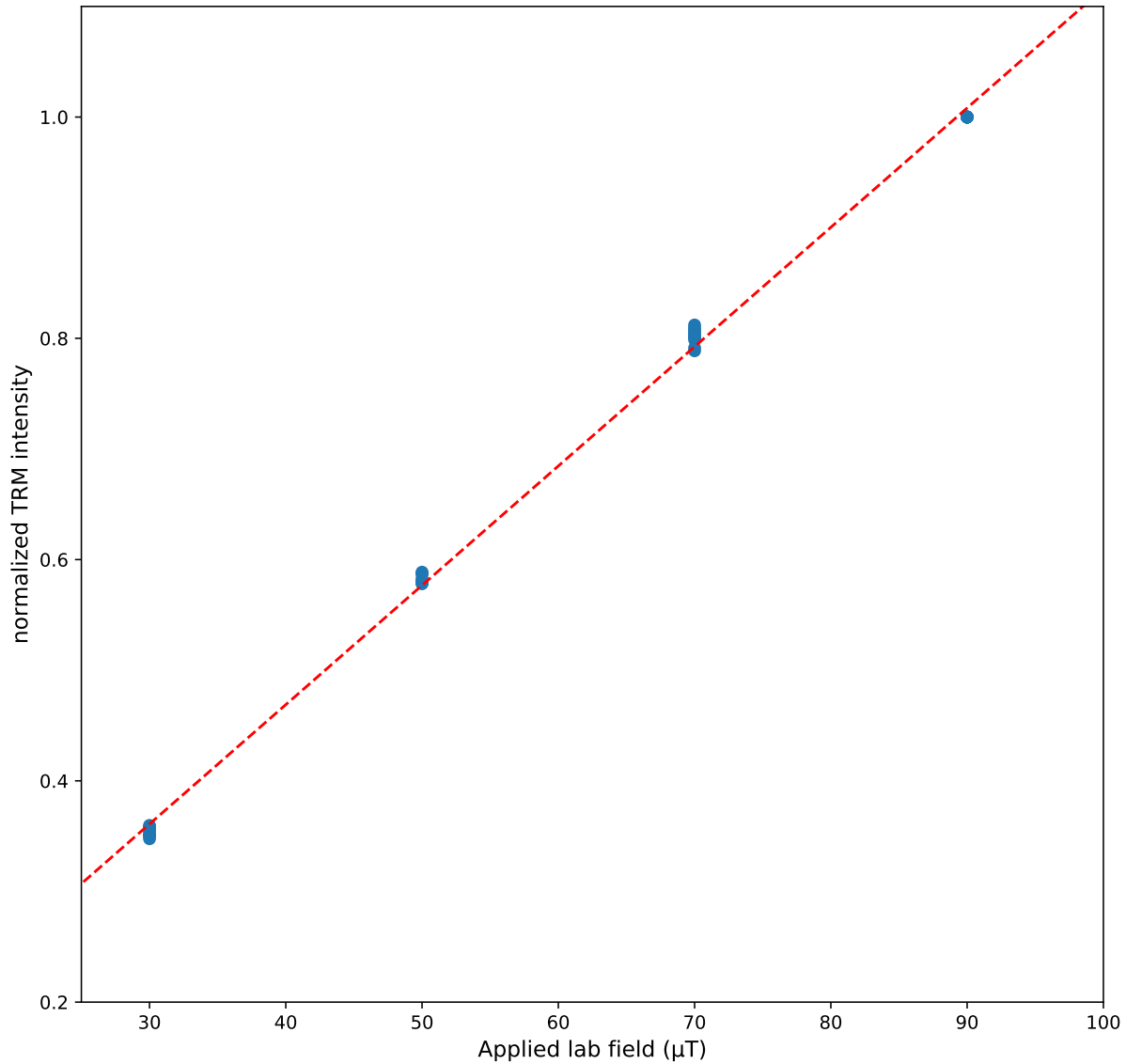


**Fig. S4.** Plot of linear thermal remanent magnetization acquisition experiment results. After IZZI-type Thellier paleointensity experiments, full TRMs were imparted on the same specimens in known lab fields of 30, 50, 70, and 90  $\mu\text{T}$ . The red dashed line shows a linear fit through the data points. The results show that the anorthosite xenoliths do not acquire saturation remanence or display non-linear remanence acquisition under fields relevant to this study. Therefore, non-linear acquisition correction is not needed for our paleointensity results.

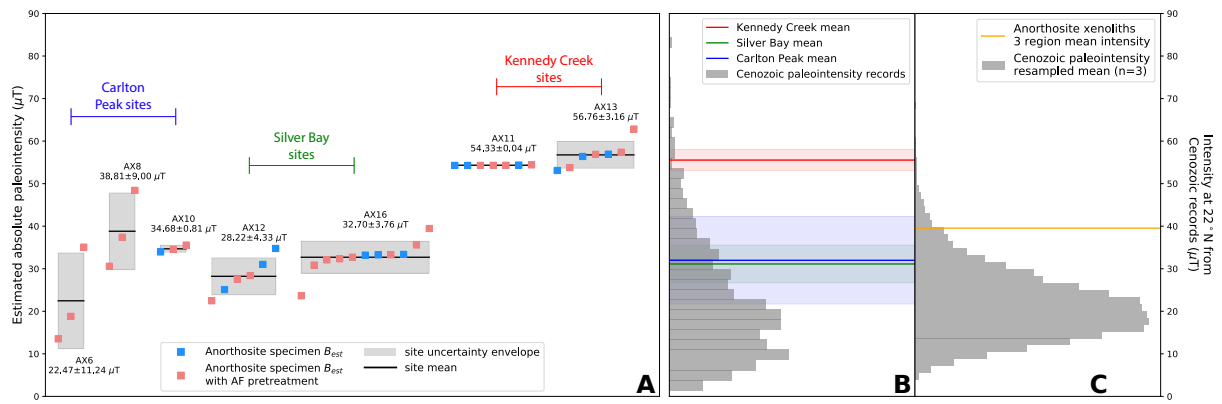


**Fig. S5.** A) Summary plot of individual specimen absolute paleointensity results (square symbols) and their averages and standard deviations at site level (black bars with grey uncertainty boxes) from this study. All results are corrected for cooling rate with a factor of 0.74. Each 'AX' site is an individual anorthosite xenolith within the Beaver River diabase. The sites with successful experiments come from 3 regions which would have cooled at distinct times yielding similar estimates within the each region with differences between regions. B) Specimen level means calculated for these regions are compared to the distribution of intensities calculated from the existing paleointensity data in the PINT database (PINT v8.0.0; <http://www.pintdb.org/>; 6) at the latitude corresponding to the paleolatitude of study region (22°N). C) The mean of the 3 regional means is compared to means calculated from 3 random values drawn from the Cenozoic data. The paleointensity records used for resampling are filtered for  $Q_{PI} \geq 3$  (7). The distribution represents a total of 10,000 iterations of taking 3 random draws and calculating the mean.

**Table S1.** Specimen paleointensity results that passed our selection. Paleointensity results for specimens that passed quality criteria.  $B_{anc}$  is the calculated ancient field intensity over the chosen temperature interval in  $\mu T$ .  $T_{min}$  and  $T_{max}$  indicate the temperature interval over which the best fit for paleointensity was defined. N is the number of steps used within the selected interval for paleointensity determination. FRAC is the fraction of remanence. NpTRM shows the number of pTRM checks within the selected interval for paleointensity determination.  $\beta$  is the scatter parameter. GAP-MAX is the maximum magnetization gap between two adjacent steps. MAD is the maximum angle of deviation. DANG is the deviation angle. SCAT is the scatter parameter. Paleolatitude is calculated from the inclination values reported in (8).  $\gamma$  is the gamma statistic that measures the angle between the last pTRM step used for paleointensity determination and the applied field direction. V(ADM) is the virtual (axial) dipole moment reported in  $10^{21} \text{ Am}^2$  ( $\text{ZAm}^2$ ).

Site	Specimen	$B_{anc}$	$T_{min}$	$T_{max}$	N	FRAC	NpTRM	$\beta$	GAP-MAX	MAD (°)	DANG (°)	SCAT	Paleolatitude	$\gamma$	V(ADM) ( $\text{ZAm}^2$ )
AX6	AX6-2a	18.25	400	585	18	0.7	10	0.04	0.12	3.44	3.43	PASS	21.97	2.7	29.34
AX6	AX6-3a	25.39	400	585	18	0.76	10	0.04	0.1	4.28	2.88	PASS	21.97	3.2	40.82
AX6	AX6-1a	47.36	475	585	15	0.6	10	0.02	0.16	2.92	1.67	PASS	21.97	2	76.13
AX8	AX8-3a	41.3	400	580	17	0.75	9	0.03	0.14	4.38	2.22	PASS	22.98	11.2	65.53
AX8	AX8-2a	50.51	400	580	17	0.63	9	0.04	0.16	3.19	1.29	PASS	22.98	3.7	80.15
AX8	AX8-1a	65.38	425	566	13	0.6	8	0.07	0.2	5.28	2.95	PASS	22.98	7	103.74
AX10	AX10-1a	45.84	425	585	17	0.78	10	0.06	0.24	5.6	2.62	PASS	20.37	4.7	75.2
AX10	AX10-2a	46.61	450	585	16	0.62	10	0.04	0.2	5.32	2.24	PASS	20.37	7.8	76.46
AX10	AX10-3a	48.01	425	585	17	0.69	10	0.04	0.24	4.02	1.56	PASS	20.37	5.8	78.76
AX11	AX11-1a	73.29	425	560	10	0.67	6	0.08	0.21	5.28	2.54	PASS	19.43	5.9	121.64
AX11	AX11-2a	73.29	400	560	11	0.65	6	0.07	0.21	3.94	1.51	PASS	19.43	9.9	121.64
AX11	AX11-4a	73.31	500	570	11	0.66	8	0.09	0.2	1.53	3.27	PASS	19.43	5.6	121.68
AX11	AX11-6a	73.32	200	562	14	0.69	7	0.07	0.17	4	1.33	PASS	19.43	3	121.69
AX11	AX11-9a	73.34	100	562	15	0.67	7	0.06	0.17	5.34	1.13	PASS	19.43	11.9	121.73
AX11	AX11-3a	73.41	400	560	11	0.66	6	0.08	0.21	3.95	2.11	PASS	19.43	8.2	121.84
AX11	AX11-5a	73.44	400	566	14	0.73	8	0.05	0.18	2.93	0.85	PASS	19.43	1.9	121.89
AX12	AX12-14a	30.34	475	585	16	0.75	10	0.06	0.17	1.74	0.55	PASS	35.73	0.9	40.86
AX12	AX12-1a	33.89	0	580	21	0.97	9	0.03	0.17	5.47	4.73	PASS	35.73	10	45.64
AX12	AX12-6a	37.18	425	564	12	0.69	7	0.08	0.22	3.64	2.05	PASS	35.73	5	50.07
AX12	AX12-8a	38.34	475	565	12	0.75	8	0.06	0.25	1.46	2.29	PASS	35.73	1.6	51.63
AX12	AX12-4a	41.89	500	585	14	0.66	10	0.05	0.24	3.85	3.19	PASS	35.73	11.4	56.42
AX12	AX12-2a	46.94	425	570	14	0.7	8	0.05	0.24	3.39	2.38	PASS	35.73	7	63.22
AX13	AX13-3a	71.68	100	550	12	0.71	5	0.08	0.22	5.92	1.88	PASS	19.36	3.4	119.07
AX13	AX13-7a	72.6	475	585	15	0.61	10	0.03	0.2	3.62	2.09	PASS	19.36	11.6	120.6
AX13	AX13-4a	76.13	200	550	11	0.65	5	0.04	0.18	8.82	1.07	PASS	19.36	3.7	126.47
AX13	AX13-6a	76.8	200	555	12	0.7	6	0.06	0.22	3.82	1.53	PASS	19.36	4.5	127.58
AX13	AX13-2a	76.86	200	555	12	0.71	6	0.05	0.2	8.08	2.23	PASS	19.36	4.1	127.68
AX13	AX13-9a	77.48	0	564	17	0.94	7	0.03	0.16	5.96	1.07	PASS	19.36	2.6	128.71
AX13	AX13-8a	84.83	450	570	13	0.81	8	0.02	0.24	3.69	1.82	PASS	19.36	5.1	140.92
AX16	AX16-15a	31.91	475	570	13	0.61	8	0.07	0.17	3.07	1.41	PASS	30.08	2.6	46.16
AX16	AX16-13a	41.68	400	570	15	0.72	8	0.07	0.2	3.47	1.85	PASS	30.08	1.1	60.29
AX16	AX16-16a	43.3	400	562	13	0.65	7	0.09	0.18	5.14	2.94	PASS	30.08	2	62.63
AX16	AX16-14a	43.64	400	565	14	0.63	8	0.08	0.14	3.84	2.12	PASS	30.08	6	63.13
AX16	AX16-11a	44.17	450	570	14	0.7	8	0.06	0.15	2.86	2.07	PASS	30.08	4.6	63.89
AX16	AX16-4a	44.82	425	575	15	0.76	9	0.05	0.21	4.77	1.08	PASS	30.08	4.2	64.83
AX16	AX16-1a	44.9	200	564	15	0.87	7	0.06	0.22	5.56	2.4	PASS	30.08	4.5	64.95
AX16	AX16-5a	44.91	425	560	10	0.65	6	0.1	0.24	7.42	3.9	PASS	30.08	4	64.96
AX16	AX16-2a	45.05	425	564	12	0.65	7	0.07	0.22	4.25	1.44	PASS	30.08	4.9	65.17
AX16	AX16-9a	48.04	500	585	15	0.61	10	0.04	0.17	2.98	1.23	PASS	30.08	4.3	69.49
AX16	AX16-10a	53.27	510	585	14	0.62	10	0.04	0.2	2.75	1.1	PASS	30.08	5.5	77.06

**Table S2.** Summary statistics for the  $Q_{PI}$  quality criteria of (7).

Site	N	Age (Ma)	Method	AGE	STAT	TRM	ALT	MD	ACN	TECH	LITH	QPI
AX6	3	1091.8	T+	1	0	1	1	1	1	0	0	5
AX8	2	1091.8	T+	1	0	1	1	1	1	0	0	5
AX10	3	1091.8	T+	1	0	1	1	1	1	0	0	5
AX11	7	1091.8	T+	1	1	1	1	1	1	0	0	6
AX12	6	1091.8	T+	1	1	1	1	1	1	0	0	6
AX13	7	1091.8	T+	1	1	1	1	1	1	0	0	6
AX16	11	1091.8	T+	1	1	1	1	1	1	0	0	6

**Table S3.** Summary paleointensity result statistics at site-level, region-level, and overall arithmetic means. The statistics names are the same as in Table S1. n represents the total number of specimen- or site- or region-level results used for calculating mean values.  $\text{inc}_{tc}$  is the tilt-corrected mean inclination. Site-level means for AX6, AX8, AX10, AX11, AX12, AX13, AX16 are calculated based on specimen results. Regional means for Carlton Peak, Kennedy Creek, and Silver Bay are calculated by grouping specimen results from AX6 and AX8 and AX10, AX11 and AX13, AX12 and AX16, respectively. Overall site mean values are calculated using all site-level results in this table. Overall region-mean values are calculated using all regional mean results in this table.

		$B_{anc}$	n	FRAC	GAP-MAX	MAD ( $^{\circ}$ )	DANG ( $^{\circ}$ )	$\text{inc}_{tc}$	$\gamma$	VDM ( $Z\text{Am}^2$ )
specimen mean for sites	AX6	30.33	3	0.69	0.13	3.55	2.66	38.9	2.63	48.76
	AX8	52.4	3	0.66	0.17	4.28	2.15	40.3	7.3	83.14
	AX10	46.82	3	0.7	0.23	4.98	2.14	36.6	6.1	76.81
	AX12	38.1	6	0.75	0.22	3.26	2.53	55.2	5.98	51.31
	AX16	44.15	11	0.68	0.19	4.19	1.96	49.2	3.97	63.87
	AX11	73.34	7	0.68	0.19	3.85	1.82	35.2	6.63	121.73
	AX13	76.63	7	0.73	0.2	5.7	1.67	35.1	5	127.29
specimen mean for regions	Carlton Peak	43.18	9	0.68	0.17	4.27	2.32	38.6	5.34	69.57
	Kennedy Creek	74.98	14	0.7	0.2	4.78	1.74	35.15	5.81	124.51
	Silver Bay	42.02	17	0.71	0.2	3.86	2.16	51.32	4.68	59.43
overall site mean		51.68	7							81.84
overall region mean		53.39	3							84.5

12 **References**

- 13 1. B Cych, M Morzfeld, L Tauxe, Bias corrected estimation of paleointensity (BiCEP): An improved methodology for obtaining  
14 paleointensity estimates. *Geochem. Geophys. Geosystems* **22** (2021).
- 15 2. Y Arai, Secular variation in intensity of the past geomagnetic field. *M.Sc. thesis, Univ. Tokyo, Tokyo, Jpn.* (1963).
- 16 3. GA Paterson, A simple test for the presence of multidomain behavior during paleointensity experiments. *J. Geophys. Res.*  
17 **116** (2011).
- 18 4. EJW Verwey, Electronic Conduction of Magnetite ( $\text{Fe}_3\text{O}_4$ ) and its Transition Point at Low Temperatures. *Nature* **144**,  
19 327–328 (1939).
- 20 5. SL Halgedahl, R Day, M Fuller, The effect of cooling rate on the intensity of weak-field trm in single-domain magnetite. *J.*  
21 *Geophys. Res. Solid Earth* **85**, 3690–3698 (1980).
- 22 6. RK Bono, et al., The PINT database: A definitive compilation of absolute palaeomagnetic intensity determinations since 4  
23 billion years ago. *Geophys. J. Int.* (2021).
- 24 7. AJ Biggin, GA Paterson, A new set of qualitative reliability criteria to aid inferences on palaeomagnetic dipole moment  
25 variations through geological time. *Front. Earth Sci.* **2** (2014).
- 26 8. Y Zhang, NL Swanson-Hysell, MD Schmitz, JD Miller, MS Avery, Synchronous emplacement of the anorthosite xenolith-  
27 bearing Beaver River diabase and one of the largest lava flows on Earth. *Geochem. Geophys. Geosystems* (2021).